Raman spectroscopy study of C-O-H-N speciation in reduced basaltic glasses: implications for reduced planetary mantles

Celia Dalou[1,2*], Marc M. Hirschmann[2], Steven D. Jacobsen[3] , and Charles Le Losq[4]

[1.] Centre de Recherches Pétrographiques et Géochimiques, 15 rue Notre-Dame des Pauvres, BP20, 54501 Vandoeuvre-lès-Nancy Cedex, France

[2.] Dept. of Earth Sciences, 108 Pillsbury Hall, University of Minnesota, Minneapolis, MN 55455, USA

[3.] Department of Earth and Planetary Sciences, Northwestern University, Evanston, IL 60208, United States

[4.] Research School of Earth Sciences, The Australian National University, Building 142, Mills Road, Canberra ACT 2601, Australia

*cdalou@crpg.cnrs-nancy.fr

Keywords: magma ocean, volatiles, oxygen fugacity, nitrogen, carbon, hydrogen, Raman spectroscopy.

Abstract

To better understand the solution of volatile species in a reduced magma ocean, we identify via Raman spectroscopy the nature of C-O-H-N volatile species dissolved in a series of reduced basaltic glasses. The oxygen fugacity (f_{O2}) during synthesis varied from highly reduced at two log units below the iron-wustite buffer (IW-2.1) to moderately reduced (IW-0.4), spanning much of the magmatic f_{O2} conditions during late stages of terrestrial accretion. Raman vibrational modes for H_2, NH_2^-, NH_3, CH_4, CO, CN^-, N_2, and OH^- species are inferred from band assignments in all reduced glasses. The integrated area of bands assigned to N_2, CH_4, NH_3 and H_2 vibrations in glasses increases with increasing molar volume of the melt, whereas that of CO decreases. Additionally, with increasing f_{O2}, CO band areas increase while those of N_2 and NH_3 decrease,

suggesting that the solubility of these neutral molecules is not solely determined by the melt molar volume under reduced conditions. Coexisting with these neutral molecules, other species as CN^- NH_2^- and OH^- are chemically bonded within the silicate network. The observations indicate that under reduced conditions 1) H_2, NH_2^-, NH_3, CH_4, CO, CN^-, N_2, and OH^- species coexist in silicate glasses representative of silicate liquids in a magma ocean 2) their relative abundances dissolved in a magma ocean depend on melt composition, f_{O2} and the availability of H and, 3) metal-silicate partitioning or degassing reactions of those magmatic volatile species must involve changes in melt and vapor speciation, which in turn may influence isotopic fractionation.

1. INTRODUCTION

Magma oceans are expected during the late stages of Earth's accretion (e.g., Elkins-Tanton, 2012) and these large-scale melting events are likely to have produced multiple episodes of volatile degassing to a primitive Hadean atmosphere (Zahnle et al. 2007; Hirschmann 2012; Tucker and Muckhopadhyay 2014). The character of this very early atmosphere remains poorly constrained, but was influenced in part by the redox state of the shallow portion of the magma oceans as they degassed (Hirschmann 2012). Redox conditions in magma oceans are likely to have evolved together with melting depth and the compositions of accreting bodies (Rubie et al. 2011). Recent models have argued for conditions ranging between -4 log units from the iron-wüstite (IW) oxybarometer (~IW-4; Rubie et al. 2011) to ~IW-1 (Siebert et al. 2013), but these apply to conditions at the locus of equilibration between silicate melt and core-destined metal. Degassing occurred shallower in the magma column, where redox conditions may have been different (Hirschmann 2012; Zhang et al. 2017) and this may have had important control on the nature of dissolved C-O-H-N species, which in turn influenced the outgassing of the nascent Hadean atmosphere.

The dissolution of C-O-H-N in melts under reducing conditions is known to be complex, involving combinations of H, O-H, C-O, and C-H species (Mysen and Vogel 2010; Hirschmann 2012; Ardia et al. 2013; Dasgupta et al. 2013; Armstrong et al. 2015; Kadik et al. 2013, 2015, 2017) (Table S1). Speciation of N seems to be particularly

intricate, involving multiple of N-H species, N_2 molecules, and nitride ions (Libourel et al. 2003; Mysen and Fogel 2010; Kadik et al. 2013; 2015; 2017; Mosenfelder et al. 2019) (Supplementary information, Table S-1).

In this study we present a series of C-O-H-N- bearing basaltic glasses quenched from high pressure and temperature (1–3 GPa and 1400–1600 ºC) synthesized over a range of reduced conditions (IW-2.1 to IW -0.4) representative of the late stages of magma oceans. Though magma oceans should be ultramafic, challenges in quenching such low viscosity liquids lead us to use basaltic compositions as approximate analogs. In the range of f_{O2} studied (IW-0.4 to IW-2.1 Table 1), the "total H" content and C content increase, whereas N content decreases with increasing f_{O2} (Fig. 1). However, these C-O-H-N- bearing basaltic glasses are not vapor saturated, instead their H, C and N contents are controlled by equilibrium exchange with a metal alloy (Dalou et al. 2017). Moreover, analytical determinations of H, C and N concentrations does not reveal the underlying distribution of C-O-H-N species (for instance, OH-, H_2, CH_4 and NH_3 likely contribute to "total H"). Therefore to better understand controls on H, C and N speciation in reduced basaltic glasses, we present Raman spectroscopic observations, which place new constraints on the magmatic speciation of C-O-H-N species under reduced conditions. Note that for the different individual species detected in the reduced glasses, Raman cross-sections are expected to vary. Thus, the band areas observed give relative but qualitative species abundances.

The speciation of volatiles in amorphous silicate changes with temperature and during quench (e.g. Nowak and Behrens 1995; Nowak et al. 2003). For instance, temperature-dependent speciation changes are known for dissolved H_2O and CO_2, whereby the reactions

$$H_2O(melt) + O^{2-}(melt) \leftrightarrow \square 2OH^-(melt) \quad (1)$$

$$CO_2(melt) + O^{2-}(melt) \leftrightarrow \square CO_3^{2-}(melt) \quad (2)$$

shift to the left with decreasing temperature. Nevertheless, speciation is frozen-in below the glass transition temperatures (e.g. Sowerby and Keppler 1999). To our knowledge, such effects on N-O-H species has not been determined, but temperature effects are probable. Although we cannot ascertain the magnitude of such effects on the glasses studied in this work, 1) results from Mysen and Fogel (2010) show that the speciation

differences in the melts at *HT* and at their glass transition temperature are small; and 2) C-O-H-N species silicate melts observed by Raman spectroscopy *in situ* during hydrothermal diamond anvil cell experiments (e.g. Mysen 2015; Mysen 2016; Mysen 2018) are in qualitative agreement with the speciation of H, C and N presented below. However, these HDAC experiments do not permit observation of speciation below the IW buffer or for silicate melt compositions representative of planetary magma oceans (Mysen 2015; Mysen 2016; Mysen 2018). Here we explore the interaction between different C-O-H-N individual species in reduced basaltic glasses using variations in Raman band areas, and examine the influence of P, T, and f_{O2}, H_2 relative proportion, and glasses' molar volume of the melt on the speciation of H, C and N.

2. METHODS

Experimental Methods

The glasses in this study were synthesized and characterized by electron probe microanalysis (EPMA) and secondary ion mass spectrometry (SIMS) by Dalou et al. (2017). Starting synthetic basaltic compositions include one based on the Adirondack-class Humphrey basalt (noted HB) from Gusev Crater, Mars, close in composition to that used by Stanley et al. (2014) and and Armstrong et al. (2015) and another similar to the normal MORB composition (noted MORB) used by Armstrong et al. (2015). Following mixing of base basalt powder compositions, variable amounts of Fe_4N and Si_3N_4 were added as N sources; the graphite capsules from high-pressure experiment provided the source of C. Oxygen fugacity (fO_2) was varied (but not controlled) by varying the amount of Si_3N_4 added to starting compositions, based on the reaction:

$$6\,FeO_{melt} + Si_3N_{4\ nitride} = 6\,Fe_{alloy} + 3\,SiO_{2\ melt} + 2\,N_{2\ melt\ or\ alloy} \quad (3)$$

The high-pressure experiments were designed to equilibrate graphite saturated basaltic glasses with Fe-C-N alloys over a range of redox conditions (IW-0.4 to IW-2.1, Table 1). No water was deliberately introduced and f_{H2O} was not fixed, but measured "H" in the samples (Table 1) results from contamination of the starting materials and from H_2O introduced during piston cylinder experiments (e.g., Médard et al. 2008). Although

H, C, and N concentrations in the melt varied depending on the experimental f_{O2} (Table 1), in no cases were they saturated, as no vapor bubbles are apparent in the quenched samples.

Experiments were performed in a piston cylinder apparatus at 1.2, 2, or 3 GPa and 1400 or 1600 ºC (Table S-1). Up to 6 compositions were loaded simultaneously into individual 0.8- to 1.2-mm-diameter holes drilled into a single graphite rod. Following analysis by EPMA and SIMS, reported in Dalou et al. (2017), the gold coating was removed and samples were cleaned and dried for analysis by Raman spectroscopy.

Analytical methods

Major element and N concentrations of silicate glasses determined by EPMA, as well as C and total H, (reported as "H_2O", but including OH^-, H_2O, NH_x, CH_x, and H_2 species) determined by SIMS (Table 1), are documented in Dalou et al. (2017).

Raman spectroscopy was conducted using a custom-built, confocal micro-Raman system that includes a 458 nm solid-state diode laser source (Melles Griot 85-BLS-601) with 300 mW output. The laser intensity was reduced with neutral density filters to 10 mW power at the sample through a 100x Mitutoyo M Plan Apo objective lens with 6 mm working distance and 0.7 numerical aperture. The use of the 100x objective allowed a spatial resolution of 1-2 μm. Compared to a more conventional green-laser excitation system, use of a 458 nm (blue) excitation source not only improves the intensity of the Raman scattering, but also positions molecular vibrations from volatile species in the 2000-4000 cm^{-1} region in the mid-part of the visible region, where the Andor Newton DU970 CCD camera used to collect the spectra has ~95% quantum efficiency. Scattered light was collected through a confocal aperture into a 0.3 m focal length Andor Shamrock spectrometer with 1200 lines per mm holographic grating, with the spectral window centered at 1250 cm^{-1} and 3400 cm^{-1} for low and high wavenumber measurements, respectively. The spectral resolution ranges from 1.2-1.8 cm^{-1} at 0-3500 cm^{-1} Raman shift. Spectra were obtained for 30 seconds, averaged over 10 accumulations. With these acquisition settings and reduced power of 10 mW, Raman spectra in the O-H region of a vitreous silica (v-SiO_2) glass standard (KOG, Thomas et al. 2015) containing 332(±20)

ppm H_2O by weight exhibits a signal-to-noise ratio of about 20:1.

The experiments of Dalou et al. (2017) produced glasses more reduced than IW-2.1, but Raman examination produced too much fluorescence to accurately perform background corrections (Fig. S-1). The reason for this fluorescence is not known, but is presumably owing to stabilization of a fluorescent transition metal ion at highly reduced conditions (Baert et al. 2011).

Peak fitting procedure

Baseline correction and deconvolution of Raman spectra were performed using the IGOR software package from Wavemetrics Inc.. Low and high wavenumber spectra, from 1950 to 2230 cm^{-1} and from 2380 to 4230 cm^{-1} respectively, were processed separately. A linear baseline was used for the low wavenumber part of the Raman signal, while a spline correction was fitted for the high wavenumber baseline (Fig. 2). For the fitting procedure, Raman shift, peak width, and intensity were treated as independent variables with convergence criterion based on the minimization of χ^2.

In the 1950-2550 cm^{-1} range (Fig. 3), three bands are observed at 2110, 2265, and 2330 cm^{-1}. The 2330 cm^{-1} band shows an asymmetry that could not be accounted for by using Gaussian, Voigt, nor Lorentzian functions. Instead, this feature was deconvolved into two Gaussian peaks: one at 2332 cm^{-1} and one at ~2338 cm^{-1} (Fig. 3). The 2332 cm^{-1} peak is very narrow with a FWHM (Full Width at Half Maximum) between 8 and 10 cm^{-1} (Table 2). The bands at 2110 and 2265 cm^{-1} were fitted with Gaussian peaks. To fit these bands, the position and width of the 2332 cm^{-1} peak was first fixed, and then all the variables (shift, FWHM, and band intensity) were optimized without constraint.

In the 2800–4400 cm^{-1} region of the Raman spectra (Fig. 2), multiple peaks are observed. In the interval between 2850-2900 cm^{-1}, two peaks can be fitted, in agreement with Mysen (2015). The broad asymmetric peak with maximum intensity around 3550 cm^{-1} is well-approximated by two Gaussian bands, with one centered between 3450 and 3530 cm^{-1} and the other at 3580 cm^{-1}, following Foustoukos and Mysen (2012). Mysen and Fogel (2010) fit the three sharp peaks spanning 3100 to 3400 cm^{-1} with three bands. In contrast, Kadik et al. (2015) employed four bands to match Raman shifts observed in

the same interval. Obtaining a fit for this portion of the spectra that matched observations to within 5-10% required four peaks near 3180, 3250, 3280, and 3350 cm^{-1} (while fitting three bands in this portion produced an intensity difference between the spectra and the fit higher than 20%). Finally, a peak around 4130 cm^{-1} is also fitted with two Gaussian peaks: one at 4130 cm^{-1} and a second at 4200 cm^{-1}. In some of the spectra this high wavenumber feature appears simply as single asymmetric band, and in others, two clearly distinguishable peaks are evident. The centroid and width of these two peaks were guided by those spectra for which the clearly distinguishable peaks could be present.

In total, ten peaks were fitted from the observed spectra. Preliminary fits of individual bands were carried out with Raman shift and FWHM as fixed variables based on previous work from Mysen (2015) for the 2800-2900 cm^{-1} portion, from Kadik et al. (2015) for the 3100 to 3400 cm^{-1} region and from Foustoukos and Mysen (2012) for the 3450-3700 cm^{-1} region. In successive refinements, the preliminary fit was used with FWHN left unconstrained and in the final step, all variables were unconstrained. The fits were judged satisfactory when the intensity difference between the spectra and the fits was less 5% for spectra with low noise, i.e. a signal-to-noise ratio of about 2.5:1 on weak bands around 2870 and 4130 cm^{-1}. For spectra corresponding to f_{O2} between IW-1.8 and IW-2.1 with a lower signal-to-noise ratio, the best fits were achieved with a fit to spectra difference between 5 and 10%.

3. RESULTS

Raman Peak assignment

The peaks at 2110 and 2230 are assigned to triple bonded C ≡ O stretching (Wetzel et al. 2013; Yoshioka et al. 2015), and triple bonded N_2 stretching (Lofthus and Krupenie 1977), respectively. Although the 2330 cm^{-1} (N_2 stretching) peak is commonly attributed to atmospheric N_2 (Klimm and Bortcharnikov 2010; Li et al. 2015a, 2017), in the glasses in this study the feature arises in part from dissolved nitrogen (Fig. 2), as also noted by Roskosz et al. (2006) and Kadik et al. (2013). A weak, although not

insignificant, peak appears between 2260 and 2275 cm^{-1} (Fig. 3). This peak cannot be attributed to a nitrosyl group (-NO) vibration, which is found in the range 2050-2100 cm^{-1} in silicate glasses (Roskosz et al. 2006). Instead, it could correspond to triple bonded C $\equiv$ N stretching (Socrates 2001). Indeed, $\nu(C \equiv N)$ band is detected at 2258 cm^{-1} in cyanamide, at 2261 cm^{-1} in malononitrile and at 2274 cm^{-1} in cyanoacetamide (Parker and Hope 2010, and references therein).

The two peaks at 2860 and 2900 cm^{-1} (Fig. 5a and b) are assigned to C-H stretching in agreement with ^{13}C magic angle spinning nuclear magnetic resonance data on C-O-H-bearing aluminosilicate glasses (Mysen et al. 2011). The peak at 2900 cm^{-1} is assigned to C-H stretching in CH_4 (e.g. Ardia et al. 2013; Mysen 2015). The assignment of the peak around 2870 cm^{-1} is often assigned to C-H stretching vibration in Si-CH_3 (Mysen and Yamishita 2010; Mysen 2015).

The broad asymmetric peak with maximum intensity around 3550 cm^{-1} is assigned to OH^- stretching vibrations. As observed in hydrous glasses, this peak extends between 2800 and 4000 cm^{-1} (e.g., McMillan and Remmele 1986; Frantz et al. 1993), forming the background below the peaks assigned to N-H and C-H stretching (Fig. 2). Its asymmetry results from the complex bonding of water in silicate glasses (e.g. Le Losq et al. 2015). The Gaussian band centered near 3530 cm^{-1} assigned to isolated OH^- groups and the other near 3450 cm^{-1} is assigned to isolated and hydrogen-bonded OH^- groups (Foustoukos and Mysen 2012).

The four peaks near 3180, 3250, 3280, and 3350 cm^{-1} are assigned to N-H stretching (Roskosz et al. 2006; Mysen et al. 2008; Kadik et al. 2017). Contrary to Lautié et al. (1976)'s study which suggests that NH stretching frequency is primarily controlled by hydrogen bond strength, hydrogen bonding is very weak compared to iono-covalent bonds, especially in silicate melts. Instead, at given temperature, melt structure plays a significant role. For example, the O...O distances along the O-H...O bond affect the O-H band position (Le Losq et al. 2015). For N-H bonding, the four different bands related to N-H stretching likely correspond to different NH chemical groups (e.g. NH_2^- and/or NH_3). Nevertheless, based on both Raman and FTIR studies, the assignment of these bands to NH_2^- and/or NH_3 is not straightforward and still debated (Mysen et al. 2008; Mysen and Fogel 2010; Kadik et al. 2015, 2017; Mosenfelder et al. 2019). Mosenfelder et

al. (2019) suggest that the bands near 3225 and 3370 cm^{-1} are NH_2^- stretching vibrations, the one at 3285 cm^{-1} is an NH^{2-} stretching vibration and that the one near 3180 cm^{-1} is an overtone of the bending mode of NH_2^-. In contrast, Mysen et al. (2008) and Mysen and Fogel (2010) assigned the 3310-3320 cm^{-1} band to isolated NH_3 molecules. Some of the reasoning from Mosenfelder et al. (2019) is based on FTIR features in the 1400-1600 cm^{-1} region, but the Raman spectra in this region don't provide similar confirmatory observations, in part because these bands are weak in Raman spectra and also in the present case, the 1400-1600 cm^{-1} region has interferences from graphite and diamond vibrations (Fig. S-2), which are likely produced by graphite microinclusions (observed under reflective light, with a 100x objective) and diamond polishing powder, respectively.

The high intensity of N-H stretching bands and the large number of Raman spectra available in this study allows observations of inter-correlations between band intensities. Among the four peaks related to N-H stretching vibrations, we observe positive correlations between the 3180 and 3285 cm^{-1} bands and between the 3235 and 3355 cm^{-1} bands (Fig. 4), suggesting that these two sets of bands may each correspond to the same N-H molecules. For each correlated pair, the highest energy band (3285 and 3355 cm^{-1}) should correspond to asymmetric stretching vibrations, while the second bands (3180 and 3235 cm^{-1}) correspond to symmetric stretching (e.g., Lin-Vien et al. 1991, pp. 160-173). In zincate diamide (Richter et al. 2015) and in sulfanilamide compounds (Muthuselvi et al. 2017), a band at 3248-3250 cm^{-1} with a strong Raman intensity but very weak in FTIR is assigned to an NH_2^- symmetric stretching vibration. Its corresponding asymmetric vibration is detected at 3355 cm^{-1} by Muthuselvi et al. (2017). This assignment to NH_2^- is consistent with Mosenfelder et al. (2019).

In contrast, the origin of the bands at 3285 and 3180 cm^{-1} is less certain. The correlation in the intensities of these bands (Fig. 4a) may not support their assignment to distinct species (e.g., 3285 cm^{-1} to NH^{2-} stretching vibration and 3180 cm^{-1} to an overtone of the bending mode of NH_2^-; Mosenfelder et al. 2019), though the correlation alone also does not exclude these assignments. An additional consideration is that the bands at 3180 and 3285 cm^{-1} are narrower than those at 3235 and 3355 cm^{-1} (Table 2), which, following the logic of Mysen et al. (2008) could suggest that bands at 3180 and 3285 cm^{-1}

correspond to uncharged free NH_3 molecule (see also Nakamoto 2009, p. 159, 220). However, Mosenfelder et al. (2019) did not observe in FTIR the degenerate deformational mode at 1627 cm^{-1} that would be expected for isolated NH_3 molecules. Nevertheless, this NH bending mode of ammonia expected in the 1627 cm^{-1} region is not always observed in NH_3-bearing silica glasses (Cant and Little 1964). Further investigations are therefore necessary to assign the 3180 and 3285 cm^{-1} bands.

Consistent with the conclusions of Mysen et al. (2008) and Mosenfelder et al. (2019), there are no features detected in the Raman spectra of our glasses that correspond to NH_4^+ vibrations. These would include symmetric stretching vibration near 3470 and 3630 cm^{-1} and overtones at 2880, 3030, and 3115 cm^{-1} found in NH_4^+-bearing phases (Dong et al. 2007; Watenphul et al. 2009, and references therein).

The band near 4130 cm^{-1} is assigned to molecular H_2 (Hirschmann et al. 2012). The asymmetry of the H_2 band (Fig. 5) could reflect substitutions in multiple local environments in the silicate network, as previously suggested by Schmidt et al. (1998). This reasoning may also apply to the observed asymmetry of the N_2 band, mentioned above.

4. DISCUSSION

4.1 C-O-H-N dissolution in reduced basaltic glasses

In the reduced glasses from this study, carbon was detected as C-H complexes, CO and CN (Figs. 2 and 3). The vibration mode of carbonate ion CO_3^{2-}, at 1085 cm^{-1} (e.g., Morizet et al. 2013), overlaps with Si-O stretching mode and therefore could not be detected. However, carbonate is expected only in very small quantities at the reduced conditions at which these glasses were synthesized (Stanley et al. 2014; Armstrong et al. 2015). For these reduced conditions, CO is the main carbon species in anhydrous glasses and potentially also in hydrous glasses (e.g., Wetzel et al. 2013; Armstrong et al. 2015; Yoshioka et al. 2015). CO bonds in reduced silicate glasses were not detected in many previous Raman studies, including those of Mysen et al. (2009, 2011) and Mysen (2013, 2015) who studied sodium and alumino-sodium silicate glasses or Dasgupta et al. (2013)

and Chi et al. (2014), who examined basaltic glasses similar in composition (including H_2O content) and quenched from comparable pressure and f_{O2}. The Raman (and infrared active) band at 2110-2120 cm^{-1} observed by Wetzel et al. (2013) was misidentified as a CO ligand in carbonyl groups in reduced basaltic glasses, but was later shown to be molecular CO by Yoshioka et al. (2015), as adopted by Armstrong et al. (2015). Observation of CO in Wetzel et al. (2013), Armstrong et al. (2015), and this study may be enhanced by the use of a 458 nm (blue) excitation line as compared to the 514 nm laser used in the studies of Mysen et al. (2009, 2011), Mysen (2013, 2015), Dasgupta et al. (2013), and Chi et al. (2014). Because C ≡ O bonds are strongly polarized (electronegativity of C: 2.55 versus O: 3.44), and CO concentrations comparatively small (<120 ppm; Armstrong et al. 2015), their Raman signals are weak. As Raman scattering intensity is inversely proportional to the fourth power of the excitation laser wavelength (Long 1977), a 458 nm excitation line enhances the C ≡ O bond scattering intensity as compared to a 514 nm laser. Because CO is not easily detected, studies of C dissolution in reduced glasses have underestimated its importance and instead tended to emphasize the roles of methyl (CH_3^-) groups and molecular CH_4 (e.g., Mysen et al. 2009, 2011; Mysen and Yamashita 2010; Mysen 2013, 2015; Ardia et al. 2013; Dasgupta et al. 2013). CO is likely dissolving as:

$$C_{(graphite)} + ½\ O_{2\ (melt)} \Leftrightarrow CO_{(melt)}. \quad (4)$$

In dry reduced melts, the concentration of reduced non-carbonate C correlates with f_{CO} with a slope close to 1 (Armstrong et al. 2015). Fig. 6a and Fig. 6b show that the area of the 2120 cm^{-1} Raman band correlates with log f_{CO} (calculated as described in Armstrong et al. 2015) and log f_{O2}, respectively. This correlation supports the conclusion that CO detected in silicate glasses is not owing to pentacarbonyl $Fe(CO)_5$, (e.g., Wetzel et al. 2013; Stanley et al. 2014), but rather to isolated C≡O species (Yoshioka et al. 2015; Armstrong et al. 2015). The ionic porosity is a measure of "free volume" in the glass defined by the difference between the total molar volume and the volume of occupied by the constituent ions. Like noble gas solubilities (as Ar, Ne and He; e.g. Carroll and Stolper 1993; Paonita et al. 2000; Marrocchi and Toplis 2005; Iacono-Marziano et al. 2010), CO peak area correlates with the molar volume of the melt (Fig.

6c). Although the ionic porosity (IP) is a useful proxy of available space that can be filled by neutral gas molecules, quite different values of IP can be calculated depending on the method used (e.g. Carroll and Stolper 1993; Paonita et al. 2000; Marrocchi and Toplis 2005; Iacono-Marziano et al. 2010). Therefore, we chose to use molar volume of the melt, expressed in cm^3/mole, which offers a more direct comparison among literature data, as its calculation depends simply on glass compositions, *P* and *T*. In this particular case, correlations between CO peak area and position and molar volume are consistent with the interpretation that it arises from C≡O stretching in a neutral molecule with a dipole moment that interacts weakly with the silicate matrix (Yoshioka et al. 2015). Contrary to that of other neutral molecules like N_2, CH_4, NH_3 and H_2 (see following discussion), the CO band area decreases with molar volume (Fig. 6c).

C-H vibrations have intense Raman signals, even at low concentrations (Ardia et al. 2013; Chi et al. 2014). Methane forms with as little as 400 ppm water in silicate glasses (Li et al. 2015b; Armstrong et al. 2015) and remains stable from moderately (IW-0.4) to very reduced conditions (IW-3; Ardia et al. 2013; Kadik et al. 2015, 2017). As Mysen and Yamashita (2010), Mysen et al. (2011) and Mysen (2015), we observed two peaks at 2860 and 2900 cm^{-1} corresponding to C-H vibrations (Fig. 5a and b). The peak at 2900 cm^{-1} is more intense and is assigned to C-H vibration in CH_4 (Mysen et al. 2009 and references therein). Although Mysen and Yamashita (2010), Mysen et al. (2011) and Mysen (2015) assigned the peak around 2870 cm^{-1} to C-H stretching in Si-CH_3, this complex is unlikely to be stable at high-temperature (e.g. Renlund et al. 1991). In addition, the linear increase of the area of the peak 2860 cm^{-1} with the increasing molar volume (Fig. 6d) suggests that this peak more likely corresponds to C-H stretching in CH_4. Consequently, the presence of two different peaks C-H stretching in CH_4 more likely reflects multiple local environments in the silicate network, as it was observed for N_2 and H_2.

We observe positive linear correlations between the peak areas of CH_4 relative to that of OH (A_{CH}/A_{OH}) and the peak area assigned to H_2 (Fig. 6e). Under reducing conditions, CH_4 likely dissolves as:

$$C_{(graphite)} + H_{2\,(melt)} + 2OH^-_{(melt)} \Leftrightarrow CH_{4\,(melt)} + O^{2-}_{(melt)}. \quad (3)$$

The two distinct trends correspond to two different temperatures (1400 and 1600°C), whereas no distinction is observed for different pressures. Ardia et al.'s (2013) model showed that CH_4 solubility in reduced glasses increases with increasing H content and P, and decreasing f_{O2}. In this study, we do not observe a clear relationship between the CH_4 band area and f_{O2} (Fig. 6f), likely because we cannot directly investigate the influence of f_{O2} independently from H content.

Below IW, nitrogen is present as N-H species, N_2 and C≡N. Kadik et al. (2017) detected NH species at f_{O2} conditions down to IW-3.1 We observe a positive linear correlation between the sum of the 3180 and 3285 cm^{-1} bands with the molar volume of the melt (Fig. 7a), whereas we note an absence of any relationship with the sum of the 3235 and 3355 cm^{-1} bands with the molar volume (Fig. 7b). This implies that the 3180 and 3285 cm^{-1} bands correspond to an N-H vibration of a neutral molecule, likely NH_3, and the 3235 and 3355 cm^{-1} bands correspond to an N-H vibration of a bonded species, likely NH_2^- consistent with Mosenfelder et al. (2019). Based on a negative correlation between NH_2^-/NH_3 ratio with decreasing melt polymerization, Mysen and Fogel suggested that NH_3 interacts with bridging oxygen in the silicate melt to form Si-NH_2 and Si-OH bonds following:

$$Si\text{-}O\text{-}Si + NH_3 \Leftrightarrow Si\text{-}NH_2 + HO\text{-}Si. \quad (6)$$

This equilibrium appears unaffected by P or T and is consistent with the observed positive correlation between the peak areas of NH_2^- relative to that of OH (A_{NH2-}/A_{OH}) and the peak area assigned to NH_3 (Fig. 7c).

Dissolution of molecular N_2 in silicate glasses has been inferred indirectly based on solubility studies (Libourel et al. 2003; Miyazaki et al. 2004), and observed previously by Raman spectroscopy (Roskosz et al. 2006; Mysen and Fogel 2010; Mysen 2013; Kadik et al. 2013; Li et al. 2015a). In reduced silicate glasses, N-H bonded species are generally considered to be the main dissolved species of nitrogen (Mysen et al. 2008; Mysen and Fogel 2010; Kadik et al. 2013, 2015, 2017; Li et al. 2015a), and this provides a partial explanation for the enhanced nitrogen concentrations at reduced relative to oxidized conditions (Kadik et al. 2013, 2015; Li et al. 2016; Dalou et al. 2017). On the other hand, enhanced nitrogen solubility at reduced conditions is also observed from 100 kPa gas mixing experiments, in which N-H species cannot play a role (Libourel et al.

2003). The use of a 458 nm excitation source improves the intensity of N_2 scattering in N-rich samples, which allows the observation of variation of the N_2 vibration intensity, and which cannot be attributed to air contamination (Fig. 2b). As for CO, N_2 band area depends on molar volume of the melt, f_{O2}, P and T (Fig. 7d and e), but in contrast with CO band area, N_2 peak area increases with molar volume of the melt. Clearly, even as NH (or other nitride species) becomes important under reducing conditions (Libourel et al. 2003; Li et al. 2015a; Kadik et al. 2015; 2017; Mosenfelder et al. 2019), N_2 band intensity remains non-negligible.

We observe positive linear correlations between the peak areas of NH complexes relative to that of N_2 (A_{NH}/A_{N2}) and the peak area assigned to H_2 (Fig. 7f). In addition, Mysen and Fogel (2010) observed increasing N solubility with increasing H_2 fugacity: combined, these trends suggest the following equilibrium:

$$3H_{2\,(melt)} + N_{2\,(melt)} \Leftrightarrow 2NH_{3\,(melt)}. \quad (7)$$

The two positive linear correlations between A_{NH}/A_{N2} and A_{H2} (Fig. 7f) correspond to the two different experimental temperatures, but do not depend on pressure. The A_{NH}/A_{N2} ratio does not seem to increase with decreasing f_{O2} or H/N ratio (Fig. S-3). This implies that the equilibrium Eq. 5 depends mainly on temperature and H_2 fugacity (Mysen and Fogel 2010).

The observed C≡N vibration band at 2261-2268 cm^{-1} is weak compared to C≡O vibration band (Fig. 3), even though the C≡N bond has a moderate Raman intensity (Socrates 2001). Compared to C≡O bonds, C≡N bonds (electronegativity of C: 2.55 versus N: 3.04) are less polarized, which may suggest either that C≡N complexes are in low abundance compared to other N species in these silicate glasses, or that the C≡N band intensity is weakened by the associated bonded metal ion (e.g, X-C≡N; Colthrup et al. 1975, pp. 235-240). Nitrile groups coordinated to metal ions have C≡N stretching bands at higher wavenumber than that of C≡N bonded to O (2245-2256 cm^{-1}), C (2220-2240 cm^{-1}) or N (2210-2225 cm^{-1}) (Colthrup et al. 1975, pp. 235-240). Therefore, the

features we observe at 2261-2268 cm^{-1} are consistent with metal-cyanide complexes in the silicate network. The band area of C≡N stretching decreases significantly with the increasing f_{O2} (Fig. S-4). In addition, it decreases with increasing temperature and pressure (Fig. S-4). This may suggest that cyanide complex solubility in silicate melts increases under more reducing conditions and at lower *P*-*T*, although caution should be taken to interpret Raman band areas in term of solubility.

In anhydrous glasses quenched at 100 kPa, Libourel et al. (2003) observed a transition between the physical solubility (N dissolved as N_2 in interstitial sites) and chemical solubility of N around IW. Below IW, N is assumed to dissolve as N^{3-}, i.e., nitride ions (Libourel et al. 2003). At conditions more reducing than IW-7, the solubility of N plateaus, presumably due to saturation in TiN (Libourel et al. 2003). The dominant vibrations for nitride stretching are near 405 cm^{-1} for Ti-N (Dam et al. 2012) and near 800 cm^{-1} for Si-N (Soignard and McMillan 2004). Unfortunately, in the 300-900 cm^{-1} range, the Raman signal is dominated by T-O-T and T-O bands (Fig. S-2), so it is difficult to ascertain the presence or absence of nitride species in our glasses.

Hirschmann et al. (2012) showed that H_2 solubility depends on f_{H2} and pressure and, based on comparison between basaltic and andesitic glass compositions, that the solubility is potentially consistent with an ionic porosity dissolution mechanism. In agreement with this study, we observe a positive linear, although scattered, correlation between H_2 peak area and the molar volume of the melt (Fig. S-5), whereas no correlation is observed with the f_{O2} (Fig. S-5).

4.2 Implications for the volatile speciation in early planetary mantles

Similar to previous studies (Mysen et al. 2008, 2009; Kadik et al. 2013, 2015, 2017; Wetzel et al. 2013; Chi et al. 2014; Armstrong et al. 2015; Yoshioka et al. 2015; Li et al. 2015a; Mosenfelder et al. 2019), the Raman spectra presented here demonstrate that C-O-H-N speciation in reduced silicate glasses involves both chemically-bonded ionic complex and weakly interacting interstitial neutral molecules. Because the stability of individual species may be related to reactions with distinct dependencies on f_{O2}, f_{H2O}, melt composition, temperature and pressure, the bulk solubilities of C and N in reduced

458 glasses are complex. This explains in part why studies have found seemingly
459 contradictory evidence for the importance of different species. For example, various
460 studies have suggested greater or lesser fractions of dissolved C under reduced conditions
461 is present as methane in reduced glasses (Ardia et al. 2013; Wetzel et al. 2013; Chi et al.
462 2014; Kadik et al. 2014; Armstrong et al. 2015). C-H and N-H species solubilities may be
463 particularly intricate, given the possibilities of both ionic and neutral complexes, the latter
464 occupying interstitial sites in a manner similar to rare gases (Carroll and Stolper, 1993;
465 Iacono-Marziano et al. 2010). Neutral substitution of H_2 (Hirschmann et al. (2012), N_2
466 (Libourel et al. 2003; and CO (Armstrong et al. 2015) are also relevant. However, more
467 detailed comparison of their solubilities as a function of melt structure is needed For
468 noble gases, the influence of ionic porosity on the solubility is proportional to atomic
469 radius (Carroll and Stolper 1993). However, as the effective molecular radii of H_2 and N_2
470 are smaller than that of CO (74 and 110 pm versus 113 pm, respectively), they may be
471 more effectively incorporated in available sites than CO. NH_3 and CH_4 have much larger
472 effective radii (222 and 207 pm, respectively; Balmer et al. 2011, p. 733) and so ionic
473 species may be favored. This suggests that their solubilities are determined by more
474 complex factors than variations in available interstitial sites.
475 From a broader perspective, the complex speciation of C and N complexes under
476 reduced conditions is of considerable interest to degassing of reduced magma oceans.
477 Although conventional treatments assume that atmospheres degassed from terrestrial
478 magma oceans are oxidized and dominated by H_2O and CO_2 (Matsui and Abe 1986;
479 Zahnle et al. 2007; Elkins-Tanton 2008), reduced conditions may apply to magma oceans
480 formed during accretion of the Earth, either in early stages when a solar nebular
481 component predominated (Genda and Ikoma 2008; Hirschmann et al. 2012; Sharp 2017)
482 or, potentially, during degassing of later magma oceans associated with the Moon-
483 forming impact (Elkins-Tanton 2012; Hirschmann 2012; Schaefer and Fegley 2017;
484 Lammer et al. 2018; Lock et al. 2018). Reduced surface conditions are also expected
485 above magma oceans from smaller planetary bodies (Zhang et al. 2017). Assuming a
486 reduced MO, magmatic volatiles species H_2, NH_2, NH_3, CH_4, CO, CN, N_2, and OH can
487 coexist and degas to supply the primitive atmosphere. The main high temperature species
488 in resulting degassed atmospheres would be H_2, H_2O, CO, and NH_3, with proportions

depending on f_{O2} (Schaefer and Fegley 2010). Consequently, release of those reduced magmatic species likely involved reactions such as:

$$CO_{(MO)} \Leftrightarrow CO_{(vapor)} \quad (8)$$

$$N_{2(MO)} \Leftrightarrow N_{2(vapor)} \quad (9)$$

$$CH_{4(MO)} + 2OH^{-}_{(MO)} \Leftrightarrow CO_{(vapor)} + 3H_{2(vapor)} + O^{2-}_{(MO)} \quad (10)$$

$$N_{2(MO)} + 3H_{2(MO\ or\ vapor)} \Leftrightarrow 2NH_{3(vapor)} \quad (11)$$

$$NH_2^{-}{}_{(MO)} + H_2O_{(vapor)} \Leftrightarrow NH_{3\ (vapor)} + OH^{-}_{(MO)} \quad (12)$$

$$2SiN_{(MO)} + 8OH^{-}_{(MO)} \Leftrightarrow 2SiO_{2\ (MO)} + 2NH_{3\ (vapor)} + 4O^{2-}_{(MO)} + H_{2\ (vapor)} \quad (13)$$

A common view is of a Hadean atmosphere comprising CO_2, N_2, and H_2O, with lesser amounts of CO, CH_4, and H_2 (Miyakawa et al. 2002, and references therein). However, a reduced magma ocean would have degassed an atmosphere bearing H_2, NH_3, N_2, and CO. Such reducing atmospheres are more favourable to bioorganic synthesis than CO_2-N_2-H_2O atmospheres (REF).

The complex speciation of C-O-H-N volatiles in silicate liquids also is likely relevant to fractionation of H, C, and N isotopes during core formation and magma ocean degassing (e.g. Dalou et al. 2019). Such fractionation depends on the bonding environments of these elements, which are quite varied in the diverse possible neutral and ionic combinations. Thus, consideration of H, C, and N isotopic fractionation during planetary differentiation (Grady et al. 2004; Li et al. 2016; Wu et al. 2018; Dalou et al. 2019) should be conducted in tandem with characterization of relevant species bonding, including how these may be affected by intensive variables during magma ocean evolution and degassing.

5. Conclusions

We show that the speciation of C-O-H-N species in basaltic melts is a complex function that varies with f_{O2}, H_2 content, melt composition, temperature and pressure. Neutral species such as H_2, N_2, CO, NH_3 and CH_4 are hosted in free volumes in the silicate network. Coexisting with these neutral molecules, other species as CN^- NH_2^- and OH^- are chemically bonded. These differences between physical (H_2, N_2, CO, NH_3 and

519 CH_4) and chemical (CN^- NH_2^- and OH^-) solubility influence the saturation pressure,
520 temperature, f_{O2} and f_{H2} of those species in a MO.

521 The coexistence H_2, NH_2^-, NH_3, CH_4, CO, CN^-, N_2, and OH^- dissolved in a
522 reduced MO implies diverse reactions during volatile species degassing to primitive
523 planetary atmospheres and during their partitioning into core-forming metals. These
524 reactions involve changes in C-O-H-N speciation, potentially influencing isotopic
525 fractionations. Therefore, tracing the origin of volatile elements on Earth requires
526 knowledge of their speciation during planetary formation processes.

527

528 **Acknowledgements:** The authors thank Jed Mosenfelder and Anette von der Handt
529 for helpful and inspiring discussions, and technical support. CD thanks Giada Iacono-
530 Marziano and Antonio Paonita for their helpful insights on the ionic porosity calculation.
531 CD and MH acknowledge support from the National Science Foundation grant
532 AST1344133. SDJ acknowledges support from NSF EAR-1853521 and the David and
533 Lucile Packard Foundation.

534

535

536 # REFERENCES

537

538 Ardia P., Hirschmann M. M., Withers A. C. and Stanley B. D. (2013) Solubility of CH_4
539 in a synthetic basaltic melt, with applications to atmosphere-magma ocean-core
540 partitioning of volatiles and to the evolution of the Martian atmosphere. *Geochim.*
541 *Cosmochim. Acta* **114**, 52-71.

542 Armstrong L. S., Hirschmann M. M., Stanley B. D., Falksen E. G. and Jacobsen S. D.
543 (2015) Speciation and solubility of reduced C-O-H-N volatiles in mafic melt:
544 Implications for volcanism, atmospheric evolution, and deep volatile cycles in the
545 terrestrial planets. *Geochim. Cosmochim. Acta* **171**, 283-302.

546 Baert K., Meulebroeck W., Wouters H., Cosyns P., Nys K., Thienpont H. and Terryn H.
547 (2011) Using Raman spectroscopy as a tool for the detection of iron in glass. *J.*
548 *Raman Spectrosc.* **42**, 1789-1795.

549 Balmer, R. T. (2011) *Modern engineering thermodynamics-textbook with tables booklet.*
550 Academic Press.
551 Cant, N. W. and Little, L. H. (1964) An Infrared Study of the Adsorption of Ammonia on
552 Porous Vycor Glass. *Can. J. Chem.* **42**, 802-809.
553 Carroll, M. R. and Stolper, E. M. (1993) Noble gas solubilities in silicate melts and
554 glasses: New experimental results for argon and the relationship between solubility
555 and ionic porosity. *Geochim. Cosmochim. Acta* **57**, 5039-5051.
556 Chi H., Dasgupta R., Duncan M. S. and Shimizu N. (2014) Partitioning of carbon
557 between Fe-rich alloy melt and silicate melt in a magma ocean–implications for the
558 abundance and origin of volatiles in Earth, Mars, and the Moon. *Geochim.*
559 *Cosmochim. Acta* **139**, 447-471.
560 Colthrup N. B., Daly L. H. and Wiberly S. E. (1975) *Introduction to Infrared and Raman*
561 *Spectroscopy*. New York: Academic. 2nd Ed.
562 Dalou C., Hirschmann M. M., Von Der Handt A., Mosenfelder J. and Armstrong L.
563 S. (2017) Nitrogen and carbon fractionation during core–mantle differentiation at
564 shallow depth. *Earth Planet. Sci. Lett.* **458**, 141-151.
565 Dam D. T., Nam K. D., Song H., Wang X. and Lee J. M. (2012) Partially oxidized
566 titanium carbonitride as a non-noble catalyst for oxygen reduction reactions. *Int. J.*
567 *Hydrogen Energy* **37**, 15135-15139.
568 Dasgupta R., Chi H., Shimizu N., Buono A. S. and Walker D. (2013) Carbon solution and
569 partitioning between metallic and silicate melts in a shallow magma ocean:
570 implications for the origin and distribution of terrestrial carbon. *Geochim.*
571 *Cosmochim. Acta* **102**, 191-212.
572 Dong J. L., Li X. H., Zhao L. J., Xiao H. S., Wang F., Guo X. and Zhang Y. H. (2007)
573 Raman Observation of the Interactions between NH_4^+, SO_4^{2-}, and H_2O in
574 supersaturated $(NH_4)_2SO_4$ Droplets. *J. Phys. Chem. B* **111**, 12170-12176.
575 Elkins-Tanton L. T. (2008) Linked magma ocean solidification and atmospheric growth
576 for Earth and Mars. *Earth Planet. Sci. Lett.* **271**, 181-191.
577 Elkins-Tanton L. T. (2012) Magma oceans in the inner solar system. *Annu. Rev. Earth*
578 *Planet. Sci.* **40**, 113-139.

579 Foustoukos D. I. and Mysen B. O. (2012) D/H fractionation in the H_2–H_2O system at
580 supercritical water conditions: Compositional and hydrogen bonding
581 effects. *Geochim. Cosmochim. Acta* **86**, 88-102.
582 Frantz J. D., Dubessy J. and Mysen B. (1993) An optical cell for Raman spectroscopic
583 studies of supercritical fluids and its application to the study of water to 500°C and
584 2000 bar. *Chem. Geol.* **106**, 9-26.
585 Genda H. and Ikoma M. (2008) Origin of the ocean on the Earth: early evolution of water
586 D/H in a hydrogen-rich atmosphere. *Icarus* **194**, 42-52.
587 Grady M. M., Verchovsky A. B. and Wright I. P. (2004) Magmatic carbon in Martian
588 meteorites: attempts to constrain the carbon cycle on Mars. *Int. J. Astrobiol.* **3**,117–
589 124.
590 Hirschmann M. M. (2012) Magma ocean influence on early atmosphere mass and
591 composition. *Earth Planet. Sci. Lett.* **341**, 48-57.
592 Hirschmann M. M., Withers A. C., Ardia P. and Foley N. T. (2012) Solubility of
593 molecular hydrogen in silicate melts and consequences for volatile evolution of
594 terrestrial planets. *Earth Planet. Sci. Lett.* **345**, 38-48.
595 Iacono-Marziano, G., Paonita, A., Rizzo, A., Scaillet, B. and Gaillard, F. (2010) Noble
596 gas solubilities in silicate melts: new experimental results and a comprehensive
597 model of the effects of liquid composition, temperature and pressure. *Chem.*
598 *Geol.* **279**, 145-157.
599 Kadik A. A., Litvin Y. A., Koltashev V. V., Kryukova E. B., Plotnichenko V. G.,
600 Tsekhonya T. I. and Kononkova N. N. (2013) Solution behavior of reduced N–H–O
601 volatiles in FeO–Na_2O–SiO_2–Al_2O_3 melt equilibrated with molten Fe alloy at high
602 pressure and temperature. *Phys. Earth Planet. Inter.* **214**, 14-24.
603 Kadik A. A., Koltashev V. V., Kryukova E. B., Plotnichenko V. G., Tsekhonya T. I. and
604 Kononkova N. N. (2014) Solution behavior of C-O-H volatiles in FeO-Na_2O-Al_2O_3-
605 SiO_2 melts in equilibrium with liquid iron alloy and graphite at 4 GPa and 1550°
606 C. *Geochem. Int.* **52**, 707-725.
607 Kadik A. A., Koltashev V.V., Kryukova E. B., Plotnichenko V. G., Tsekhonya T. I. and
608 Kononkova N. N. (2015) Solubility of nitrogen, carbon, and hydrogen in FeO–

609 Na_2O–Al_2O_3–SiO_2 melt and liquid iron alloy: influence of oxygen
610 fugacity. *Geochem. Int.* **53**, 849-868.
611 Kadik A. A., Koltashev V. V., Kryukova E. B., Tsekhonya T. I. and Plotnichenko V. G.
612 (2017) Application of IR and Raman spectroscopy for the determination of the role
613 of oxygen fugacity in the formation of N–C–O–H molecules and complexes in the
614 iron-bearing silicate melts at high pressures. *Geochem. Int.* **54**, 1175-1186.
615 Klimm K. and Botcharnikov R. E. (2010) The determination of sulfate and sulfide
616 species in hydrous silicate glasses using Raman spectroscopy. *Am. Mineral* **95**,
617 1574-1579.
618 Lammer H., Zerkle A. L., Gebauer S., Tosi N., Noack L., Scherf M., Pilat-Lohinger E.,
619 Güdel M., Grenfell J. L., Godolt M. and Nikolaou A. (2018) Origin and evolution of
620 the atmospheres of early Venus, Earth and Mars. *Astron. Astrophys. Rev.* **26**, 1-73.
621 Lautié, A., Froment, F. and Novak, A. (1976) Relationship between NH stretching
622 frequencies and N… O distances of crystals containing NH… O hydrogen
623 bonds. Spectrosc. Lett. **9**, 289-299.
624 Le Losq C., Mysen B. O. and Cody G. D. (2015) Water and magmas: insights about the
625 water solution mechanisms in alkali silicate melts from infrared, Raman, and ^{29}Si
626 solid-state NMR spectroscopies. *Prog. Earth Planet. Sc.* **2**, 1-16.
627 Li Y., Huang R., Wiedenbeck M. and Keppler H. (2015a) Nitrogen distribution between
628 aqueous fluids and silicate melts. *Earth Planet. Sci. Lett.* **411**, 218-228.
629 Li Y., Dasgupta R. and Tsuno K. (2015b) The effects of sulfur, silicon, water, and
630 oxygen fugacity on carbon solubility and partitioning in Fe-rich alloy and silicate
631 melt systems at 3 GPa and 1600°C: Implications for core–mantle differentiation and
632 degassing of magma oceans and reduced planetary mantles. *Earth Planet. Sci.*
633 *Lett.* **415**, 54-66.
634 Li Y. F., Marty B., Shcheka S., Zimmermann L. and Keppler H. (2016) Nitrogen isotope
635 fractionation during terrestrial core-mantle separation. *Geochem. Perspect.* **2**, 138–
636 147.
637 Li Y., Dasgupta R. and Tsuno K. (2017) Carbon contents in reduced basalts at graphite
638 saturation: Implications for the degassing of Mars, Mercury, and the Moon. *J.*
639 *Geophys. Res. Planets* **122**, 1300-1320.

Libourel G., Marty B. and Humbert F. (2003) Nitrogen solubility in basaltic melt. Part I. Effect of oxygen fugacity. *Geochim. Cosmochim. Acta* **67**, 4123-4135.

Lin-Vien D., Colthup N. B., Fateley W. G. and Grasselli J. G. (1991) *The handbook of infrared and Raman characteristic frequencies of organic molecules.* Elsevier.

Lock S. J., Stewart S. T., Petaev M. I., Leinhardt Z., Mace M. T., Jacobsen S. B. and Cuk M. (2018). The origin of the Moon within a terrestrial synestia. J. *Geophys. Res. Planets* **123**, 910-951.

Lofthus A. and Krupenie P. H. (1977) The spectrum of molecular nitrogen. *J. Phys. Chem. Ref. Data* **6**, 113-307.

Long D. A. (1977) *Raman spectroscopy*, McGraw Hill Higher Education.

Marrocchi Y. and Toplis M. J. (2005) Experimental determination of argon solubility in silicate melts: An assessment of the effects of liquid composition and temperature. *Geochim. Cosmochim. Acta* **69**, 5765-5776.

Matsui T. and Abe Y. (1986) Evolution of an impact-induced atmosphere and magma ocean on the accreting Earth. *Nature* **319**, 303-305.

McMillan P. F. and Remmele R. L. (1986) Hydroxyl sites in SiO_2 glass; a note on infrared and Raman spectra. *Am. Mineral.* **71**, 772-778.

Médard E., McCammon C. A., Barr J. A. and Grove T. L. (2008) Oxygen fugacity, temperature reproducibility, and H_2O contents of nominally anhydrous piston-cylinder experiments using graphite capsules. *Am. Mineral.* **93**, 1838-1844.

Miyazaki A., Hiyagon H., Sugiura N., Hirose K. and Takahashi E. (2004) Solubilities of nitrogen and noble gases in silicate melts under various oxygen fugacities: implications for the origin and degassing history of nitrogen and noble gases in the Earth. *Geochim. Cosmochim. Acta* **68** 387-401.

Morizet Y., Brooker R. A., Iacono-Marziano G. and Kjarsgaard B. A. (2013) Quantification of dissolved CO_2 in silicate glasses using micro-Raman spectroscopy. *Am. Mineral.* **98**, 1788-1802.

Mosenfelder J. L., Von Der Handt A., Füri E., Dalou C., Hervig R. L., Rossman G. R. and Hirschmann M. M. (2019) Nitrogen incorporation in silicates and metals: results from SIMS, EPMA, FTIR, and laser-extraction mass spectrometry. *Am. Mineral.* **104**, 31-46.

671 Muthuselvi C., Pandiarajan S., Athimoolam S., Krishnakumar R. V. and Manikandan A.
672 (2017) Structural and Optical Properties of NLO Material: 4-Sulfamoylanilinium
673 Dihydrogen Phosphate. *Adv. Sci. Eng. Med.* **9**, 931-942.
674 Mysen, B. (2016) Experimentally-determined carbon isotope fractionation in and
675 between methane-bearing melt and fluid to upper mantle temperatures and
676 pressures. *Earth Planet. Sci. Lett.* **445**, 28-35.
677 Mysen, B. (2018) Solution mechanisms of COHN fluids in melts to upper mantle
678 temperature, pressure, and redox conditions. *Am. Mineral.***103**, 1780-1788.
679 Mysen B. O. (2013) Structure–property relationships of COHN-saturated silicate melt
680 coexisting with COHN fluid: A review of in-situ, high-temperature, high-pressure
681 experiments. *Chem. Geol.* **346**, 113-124.
682 Mysen B. O. (2015) Carbon speciation in silicate-COH melt and fluid as a function of
683 redox conditions: An experimental study, in situ to 1.7 GPa and 900°C. *Chem.*
684 *Geol.* **100**, 872-882.
685 Mysen B. O. and Fogel M. L. (2010) Nitrogen and hydrogen isotope compositions and
686 solubility in silicate melts in equilibrium with reduced (N+ H)-bearing fluids at high
687 pressure and temperature: Effects of melt structure. *Am. Mineral.* **95**, 987-999.
688 Mysen B. O. and Yamashita S. (2010) Speciation of reduced C–O–H volatiles in
689 coexisting fluids and silicate melts determined in-situ to ~1.4 GPa and
690 800°C. *Geochim. Cosmochim. Acta* **74**, 4577-4588.
691 Mysen B. O., Yamashita S. and Chertkova N. (2008) Solubility and solution mechanisms
692 of N–O–H volatiles in silicate melts at high pressure and temperature-amine groups
693 and hydrogen fugacity. *Am. Mineral.* **93**, 1760-1770.
694 Mysen B. O., Fogel M. L., Morrill P. L. and Cody G. D. (2009) Solution behavior of
695 reduced C–O–H volatiles in silicate melts at high pressure and
696 temperature. *Geochim. Cosmochim. Acta* **73**, 1696-1710.
697 Mysen B. O., Kumamoto K., Cody G. D. and Fogel M. L. (2011) Solubility and solution
698 mechanisms of C–O–H volatiles in silicate melt with variable redox conditions and
699 melt composition at upper mantle temperatures and pressures. *Geochim.*
700 *Cosmochim. Acta* **75**, 6183-6199.

Nakamoto K. (2009) *Infrared and Raman spectra of inorganic and coordination compounds, Part A: Theory and applications in inorganic chemistry,* 419p. John Wiley and Sons, Hoboken, New Jersey.

Nowak, M. and Behrens, H. (1995) The speciation of water in haplogranitic glasses and melts determined by in situ near-infrared spectroscopy. Geochimica et Cosmochimica Acta, 59(16), 3445-3450.

Nowak, M., Porbatzki, D., Spickenbom, K. and Diedrich, O. (2003) Carbon dioxide speciation in silicate melts: a restart. *Earth Planet. Sci. Lett.* **207**, 131-139.

Paonita, A., Gigli, G., Gozzi, D., Nuccio, P. M. and Trigila, R. (2000) Investigation of the He solubility in H_2O–CO_2 bearing silicate liquids at moderate pressure: a new experimental method. *Earth Planet. Sci. Lett.* **181**, 595-604.

Parker, G. K. and Hope, G. A. (2010). A Spectroelectrochemical Investigation of the Interaction of Gold with Cyano-Containing Ligands. *ECS Trans.*, **28**, 223-235.

Renlund, G. M., Prochazka, S. and Doremus, R. H. (1991. Silicon oxycarbide glasses: Part I. Preparation and chemistry. *J. Mater. Res.*, **6**, 2716-2722.

Richter T. M., Alt N. S., Schlücker E. and Niewa R. (2015) Ammonothermal Synthesis and Characterization of $Li_4[Zn(NH_2)_4](NH_2)_2$. *Z. Anorg. Allg. Chem.* **641**, 1016-1023.

Roskosz M., Mysen B. O. and Cody G. D. (2006) Dual speciation of nitrogen in silicate melts at high pressure and temperature: an experimental study. *Geochim. Cosmochim. Acta* **70**, 2902-2918.

Rubie D. C., Frost D. J., Mann U., Asahara Y., Nimmo F., Tsuno K., Kegler P., Holzheid A. and Palme H. (2011) Heterogeneous accretion, composition and core–mantle differentiation of the Earth. *Earth Planet. Sci. Lett.* **301**, 31-42.

Schaefer L. and Fegley Jr B. (2017) Redox States of Initial Atmospheres Outgassed on Rocky Planets and Planetesimals. *Astrophys. J.* **843**, 1-18.

Schmidt B. C., Holtz F. M. and Beny J.-M. (1998) Incorporation of H_2 in vitreous silica, qualitative and quantitative determination from Raman and infrared spectroscopy. *J. Non-Cryst. Solids* **240**, 91-103.

Sharp Z. D. (2017) Nebular ingassing as a source of volatiles to the terrestrial planets. *Chem. Geol.* **448**, 137-150.

Siebert J., Badro J., Antonangeli D. and Ryerson F. J. (2013) Terrestrial accretion under oxidizing conditions. *Science* **339**, 1194–1197.

Stanley B. D., Hirschmann M. M. and Withers A. C. (2014). Solubility of COH volatiles in graphite-saturated martian basalts. *Geochim. Cosmochim. Acta* **129**, 54-76.

Socrates G. (2001) *Infrared and Raman Characteristic Group Frequencies—Tables and Charts*, 347 p. Wiley, New York, 3rd ed.

Soignard E. and McMillan P. F. (2004) Raman spectroscopy of γ-Si_3N_4 and γ-Ge_3N_4 nitride spinel phases formed at high pressure and high temperature: Evidence for defect formation in nitride spinels. *Chem. Mater.* **16**, 3533-3542.

Sowerby, J. R., Keppler, H. (1999) Water speciation in rhyolitic melt determined by in-situ infrared spectroscopy. Ame. Mineral. **84**, 1843-1849.

Thomas S. M., Jacobsen S. D., Bina C. R., Reichart P., Moser M., Hauri E. H., Koch-Müller M., Smyth J. R. and Dollinger G. (2015) Quantification of water in hydrous ringwoodite. *Front. Earth Sci.* **2**, 1-19.

Tucker J. M. and Mukhopadhyay S. (2014) Evidence for multiple magma ocean outgassing and atmospheric loss episodes from mantle noble gases. *Earth Planet. Sci. Lett.* **393**, 254-265.

Watenphul A., Wunder B. and Heinrich W. (2009) High-pressure ammonium-bearing silicates: Implications for nitrogen and hydrogen storage in the Earth's mantle. *Am. Mineral.* **94**, 283-292.

Wetzel D. T., Rutherford M. J., Jacobsen S. D., Hauri E. H. and Saal A. E. (2013) Degassing of reduced carbon from planetary basalts. *Proc. Natl. Acad. Sci.* **110**, 8010-8013.

Wu J., Desch S. J., Schaefer L., Elkins-Tanton L. T., Pahlevan K. and Buseck P. R. (2018) Origin of Earth's water: chondritic inheritance plus nebular ingassing and storage of hydrogen in the core. *J. Geophys. Res. Planets* **123**, 2691-2712.

Yoshioka T., Mccammon C., Shcheka S. and Keppler H. (2015) The speciation of carbon monoxide in silicate melts and glasses. *Am. Mineral.* **100**, 1641-1644.

Zahnle K., Arndt N., Cockell C., Halliday A., Nisbet E., Selsis F. and Sleep N.H. (2007) Emergence of a habitable planet. *Space Sci. Rev.* **129**, 35-78.

762 Zhang H. L., Hirschmann M. M., Cottrell E. and Withers A. C. (2017) Effect of pressure
763 on $Fe^{3+}/\Sigma Fe$ ratio in a mafic magma and consequences for magma ocean redox
764 gradients. *Geochim. Cosmochim. Acta* **204**, 83-103.
765
766 **Figure captions**
767
768 Figure 1: Variation of a)"total H", b) C and c) N content with log f_{O2} relative to the IW
769 buffer. Concentrations from Dalou et al. (2017).
770
771 Figure 2: Examples of spline baseline corrections (dashed curve) and peak fitting in the
772 2800 to 4400 cm^{-1} portion of two Raman spectra from glasses a) B706C (0.09 wt.%, 0.50
773 wt.% "total H" and IW-1.3) and b) B727F (0.26 wt.%, 0.33 wt.% "total H" and IW-1.3).
774 The grey curves correspondsto the Raman spectra and the orange curves are the peak fits.
775 (See text for discussion of band assignments).
776
777
778 Figure 3: Examples of spline baseline corrections (dashed curve) and of peak fitting in
779 the 1950 to 2550 cm^{-1} portion of the Raman spectra of glasses B706A and B714A. The
780 black spectrum is from a pure amorphous silica standard with known H_2O content
781 (KOG from Thomas et al. 2015). As for Fig. 2, the grey curve corresponds to the Raman
782 spectra and the orange curve is the peak fit. (See text for discussion of band assignments).
783
784
785 Figure 4: Co-variation of Gaussian normalized band areas a) 3180 cm^{-1} versus 3285 cm^{-1}
786 (r^2 = 0.84) and b) 3235 cm^{-1} versus 3355 cm^{-1} (r^2 = 0.91). Error bars are 2σ. The strong
787 correlations between normalized band areas suggests that the bands belong to the same
788 N-H molecules. Those bands are assigned to a) to NH_3 and b) to NH_2^-. (See text for
789 discussion of band assignments).
790
791 Figure 5: Examples of spline baseline corrections (dashed curves) and peak fitting in the
792 a) 2800 to 3000 cm^{-1} portion of the Raman spectra of glasses B712E and glass B714D,

assigned to CH stretching vibration, and b) 4050 to 4300 cm^{-1} portion of the spectrum of glasses B707C and glass B712E, assigned to H_2 peaks. As for Fig. 2 and 3, the grey curve corresponds to the Raman spectra and the orange curve is the peak fit. In both portion of the spectra, two Gaussian bands are necessary to fit this portion of the signal adequately.

Figure 6: Panels a)-c) show variation of the normalized band area near 2120 cm^{-1} assigned to $C \equiv O$ versus a) log f_{CO}, b) log f_{O2} relative to the IW buffer, and c) the molar volume of the melt. Panel d) depicts variation of the position of the 2820 cm^{-1} band with the molar volume of the melt. Panel e) represents the variations of the sum of CH_4 bands area (sum of 2860 cm^{-1} and 2900 cm^{-1} band areas) relative to that of the sum of OH bands area (sum of 3500 cm^{-1} and 3580 cm^{-1} band areas) with H_2 band areas (sum of 4130 cm^{-1} and 4200 cm^{-1} band areas). Panel f) shows the variations of the sum of CH_4 bands area (sum of 2860 cm^{-1} and 2900 cm^{-1} band areas) with log f_{O2}. On all panels, black lines are linear regressions to guide the figure reading.

Figure 7: Evolution of the sum of band areas of a) 3180 cm^{-1} and 3285 cm^{-1} and b) 3235 cm^{-1} and 3355 cm^{-1} bands with the calculated molar volumes of the melts. Panel c) represents the variations of the sum of NH_2 band areas (sum of 3235 cm^{-1} and 3355 cm^{-1} band areas) relative to that of the sum of OH band areas (sum of 3500 cm^{-1} and 3580 cm^{-1} band areas) with NH_3 band areas (sum of 3180 cm^{-1} and 3285 cm^{-1} band areas). Panels d) and e) show the variation of the area of the sum of N_2 band area (sum of band 2330 and 2340 cm^{-1} areas) with d) the molar volume of the melt. and e) log f_{O2}. Panel f) shows the variations of the sum of NH band areas (sum of 3180, 3235, 3285 and 3355 cm^{-1} band areas) relative to that of the sum of N_2 band areas (sum of band 2330 and 2340 cm^{-1} areas) with H_2 band areas (sum of 4130 cm^{-1} and 4200 cm^{-1} band areas). On all panels, black lines are linear regressions to guide the figure reading.

Table 1
Experimental conditions, molar volume (Vm) and low-wavenumber (WN) band frequency (cm^{-1}), full-width-at-half maximum (FWHM, in cm^{-1}), and normalized area (NA) along with associated errors.

Sample	P (GPa)	T (°C)	log f_{O2}	ΔIW	H_2O (wt.%)*	C (ppm)*	N (wt.%)*	Vm	CO bands			CN bands			N_2 bands					
									WN	FWHM	NA	WN	FWHM	NA	WN	FWHM	NA	WN	FWHM	NA
B706A	1.2	1400	−10.2	−1.2	0.68(1)	78(1)	0.09(1)	21.3	2123	50	0.63(2)	2268	39	0.07(1)	2332	11	0.24(1)	2340	16	0.06(2)
B706B	1.2	1400	−10.3	−1.3	0.500(4)	70(1)	0.09(1)	21.4	2122	58	0.62(3)	2263	35	0.08(1)	2331	10	0.21(2)	2338	16	0.09(1)
B706C	1.2	1400	−9.8	−0.7	1.043(5)	110(1)	0.04(1)	20.6	2119	59	0.72(8)	2267	30	0.06(2)	2331	10	0.18(3)	2340	16	0.04(3)
B707B	2	1400	−9.3	−0.4	1.29(10)	141(11)	0.13(2)	19.8	2122	58	0.57(5)	2267	33	0.05(2)	2331	8	0.17(2)	2336	20	0.22(2)
B707C	2	1400	−9.7	−0.9	0.86(2)	101(1)	0.23(1)	20.7	2126	61	0.48(3)	2263	38	0.05(1)	2331	9	0.22(4)	2337	18	0.26(4)
B712A	2	1600	−7.9	−0.7	0.716(1)	487(1)	0.14(1)	19.9	2113	56	0.91(2)	2268	35	0.02(1)	2331	9	0.03(1)	2336	20	0.04(1)
B712C	2	1600	−8.2	−1.1	na	na	0.12(2)	20.3	2117	52	0.91(1)	2267	39	0.010(3)	2333	9	0.04(8)	2338	20	0.05(1)
B712D	2	1600	−9.1	−2.1	0.289(4)	195(2)	0.78(1)	21.3	2123	46	0.73(4)	2262	37	0.05(1)	2331	9	0.10(4)	2337	16	0.13(4)
B712E	2	1600	−8.4	−1.2	0.49(2)	258(5)	0.26(1)	20.8	2121	49	0.82(1)	2262	40	0.03(1)	2332	8	0.06(1)	2336	18	0.10(1)
B712F	2	1600	−8.0	−0.8	0.721(5)	328(71)	0.14(2)	20.1	2116	58	0.89(2)	2268	39	0.02(1)	2332	10	0.05(2)	2337	18	0.04(2)
B727A	2	1600	−8.5	−1.3	0.415(3)	212(5)	0.34(2)	21.1	2117	52	0.84(1)	2263	36	0.025(4)	2332	8	0.050(4)	2337	20	0.09(1)
B727B	2	1600	−8.3	−1.1	0.75(1)	270(16)	0.21(2)	20.8	2118	51	0.87(2)	2268	36	0.017(5)	2332	9	0.04(1)	2336	20	0.07(1)
B727C	2	1600	−8.6	−1.4	0.604(3)	192(5)	0.16(3)	21.0	*below detection*											
B727D	2	1600	−9.0	−1.8	1.02(2)	213(83)	0.19(2)	20.4	2117	53	0.82(2)	2268	31	0.031(8)	2333	8	0.053(7)	2338	21	0.09(1)
B727E	2	1600	−9.0	−1.8	0.57(1)	270(13)	0.24(1)	21.1	2119	54	0.84(2)	2274	37	0.019(6)	2333	10	0.053(1)	2338	21	0.09(2)
B727F	2	1600	−8.5	−1.3	0.33(1)	222(17)	0.26(1)	21.0	2119	55	0.89(1)	2265	34	0.012(4)	2332	10	0.053(6)	2339	17	0.05(1)
B714A	3	1600	−7.9	−0.4	na	na	0.17(2)	18.7	2112	58	0.89(2)	2262	34	0.012(4)	2332	10	0.04(1)	2337	21	0.06(1)
B714B	3	1600	−8.5	−1.1	0.493(2)	239(7)	0.43(1)	19.4	2119	57	0.81(1)	2267	33	0.012(4)	2333	10	0.072(5)	2338	22	0.11(1)
B714C	3	1600	−9.1	−1.6	0.361(4)	166(9)	1.230(2)	19.8	2125	54	0.66(4)	2268	33	0.020(4)	2332	9	0.14(2)	2339	19	0.19(2)
B714D	3	1600	−8.5	−1.1	0.59(2)	223(32)	0.38(2)	19.3	2118	59	0.82(2)	2266	31	0.012(4)	2332	9	0.05(1)	2337	19	0.11(1)

Numbers in parentheses reflect 2σ standard errors in the significant digit from best-fit results.
* From Dalou et al. (2017). Numbers in parentheses for N, H content represent one standard deviation in the significant digit.

Table 2
Experimental conditions and high-wavenumber (WN) band frequency (cm^{-1}), full-width-at-half maximum (FWHM, in cm^{-1}), normalized area (NA) along with associated errors.

Sample	P (GPa)	T (°C)	log f_{O2}	CH bands						OH bands						H_2 bands					
				WN	FWHM	NA	WN	FWHM	NA	WN	FWHM	NA	WN	FWHM	NA	WN	FWHM	NA	WN	FWHM	NA
B706A	1.2	1400	−10.2	2867	66	0.015(4)	2909	41	0.027(5)	3519	141	0.24(10)	3593	97	0.31(10)	4132	73	0.015(3)	4206	32	0.004(1)
B706B	1.2	1400	−10.3	2866	53	0.016(2)	2909	38	0.025(3)	3516	161	0.32(1)	3591	96	0.31(1)	4125	58	0.015(1)	4195	54	0.004(1)
B706C	1.2	1400	−9.8	2845	44	0.009(2)	2906	52	0.036(5)	3492	161	0.37(6)	3582	103	0.39(6)	4125	57	0.015(1)	4199	33	0.001(1)
B707B	2	1400	−9.3	2863	56	0.004(1)	2911	44	0.010(2)	3503	104	0.33(7)	3583	98	0.35(7)	4134	53	0.011(2)	4186	15	0.0001(1)
B707C	2	1400	−9.7	2866	64	0.013(2)	2914	38	0.009(1)	3522	135	0.15(7)	3592	94	0.26(7)	4128	71	0.011(2)	4204	76	0.006(1)
B712A	2	1600	−7.9	2817	21	0.002(1)	2895	88	0.05(1)	3498	147	0.25(9)	3579	96	0.33(8)	4128	65	0.006(3)	4202	41	0.0001(1)
B712C	2	1600	−8.2	2811	38	0.009(3)	2882	81	0.058(4)	3514	157	0.11(1)	3585	108	0.32(1)	4132	77	0.010(4)	4202	32	0.003(2)
B712D	2	1600	−9.1	*strong fluorescence*																	
B712E	2	1600	−8.4	2842	51	0.011(2)	2903	58	0.028(3)	3526	103	0.075(4)	3589	86	0.128(4)	4141	63	0.015(2)	4203	20	0.002(1)
B712F	2	1600	−8.0	2860	40	0.008(1)	2911	50	0.039(1)	3503	156	0.11(1)	3581	91	0.15(1)	4128	55	0.017(2)	4187	55	0.002(1)
B727A	2	1600	−8.5	2862	53	0.010(1)	2913	45	0.034(2)	3543	142	0.22(1)	3594	83	0.118(5)	4129	60	0.008(1)	4165	41	0.00026(2)
B727B	2	1600	−8.3	2862	53	0.010(1)	2914	45	0.034(2)	3523	124	0.2(1)	3588	87	0.2(1)	4133	57	0.008(2)	4196	33	0.002(1)
B727C	2	1600	−8.6	2869	46	0.013(6)	2912	41	0.042(6)	3516	132	0.25(8)	3584	88	0.30(8)	4131	45	0.007(2)	4180	40	0.001(2)
B727D	2	1600	−9.0	2865	47	0.011(2)	2913	44	0.027(7)	3551	101	0.12(4)	3591	84	0.11(4)	4133	81	0.006(6)	4207	53	0.007(3)
B727E	2	1600	−9.0	2853	56	0.013(2)	2907	47	0.019(2)	3534	144	0.11(3)	3586	91	0.13(3)	4141	67	0.006(2)	4204	37	0.007(1)
B727F	2	1600	−8.5	2862	60	0.013(8)	2913	50	0.028(8)	3464	106	0.011(1)	3600	88	0.174(2)	4131	55	0.011(3)	4194	51	0.005(3)
B714A	3	1600	−7.9	2823	24	0.003(2)	2880	71	0.04(2)	3517	132	0.21(2)	3581	97	0.3(2)	4138	79	0.002(8)	4207	25	0.003(2)
B714B	3	1600	−8.5	2850	58	0.009(1)	2913	60	0.021(1)	3496	150	0.078(3)	3585	98	0.106(2)	4121	79	0.009(1)	4184	53	0.002(1)
B714C	3	1600	−9.1	*strong fluorescence*																	
B714D	3	1600	−8.5	2871	42	0.008(5)	2919	51	0.018(5)	3493	159	0.06(1)	3580	99	0.14(1)	4136	73	0.009(1)	4194	59	0.001(2)

Sample	P (GPa)	T (°C)	NH peaks											
			WN	FWHM	NA	WN	FWHM	NA	WN	FWHM	NA	WN	FWHM	NA
B706A	1.2	1400	3183	34	0.024(4)	3236	51	0.033(8)	3285	40	0.15(2)	3361	94	0.12(2)
B706B	1.2	1400	3181	37	0.022(1)	3234	53	0.030(1)	3284	41	0.118(3)	3358	96	0.11(1)
B706C	1.2	1400	3182	34	0.010(1)	3233	54	0.020(2)	3281	45	0.053(4)	3356	87	0.07(1)
B707B	2	1400	3178	35	0.014(2)	3234	64	0.032(2)	3283	43	0.084(8)	3360	104	0.12(7)
B707C	2	1400	3183	33	0.026(3)	3234	48	0.029(6)	3286	42	0.19(2)	3361	88	0.13(1)
B712A	2	1600	3181	38	0.019(3)	3234	55	0.025(9)	3280	44	0.10(1)	3356	86	0.09(1)
B712C	2	1600	3180	39	0.033(4)	3238	50	0.044(8)	3284	43	0.170(6)	3355	81	0.118(3)
B712D	2	1600	*strong fluorescence*											
B712E	2	1600	3180	39	0.048(2)	3234	59	0.102(3)	3284	45	0.231(4)	3343	103	0.32(1)
B712F	2	1600	3181	33	0.028(2)	3247	75	0.151(5)	3286	38	0.170(3)	3345	103	0.279(3)
B727A	2	1600	3182	46	0.046(1)	3238	55	0.056(2)	3284	43	0.20(2)	3354	100	0.17(1)
B727B	2	1600	3179	41	0.043(7)	3237	67	0.066(2)	3284	42	0.21(2)	3351	110	0.17(4)
B727C	2	1600	3180	44	0.030(3)	3235	50	0.036(3)	3282	44	0.13(1)	3359	94	0.114(9)
B727D	2	1600	3181	44	0.028(7)	3235	75	0.08(2)	3285	42	0.18(2)	3355	96	0.19(5)
B727E	2	1600	3181	39	0.038(3)	3242	71	0.117(7)	3285	44	0.21(1)	3345	99	0.29(1)
B727F	2	1600	3181	41	0.035(2)	3243	70	0.11(1)	3286	39	0.277(9)	3340	103	0.28(2)
B714A	3	1600	3179	44	0.03(1)	3235	49	0.04(2)	3282	44	0.12(4)	3349	108	0.13(5)
B714B	3	1600	3183	46	0.058(1)	3237	56	0.088(2)	3288	49	0.322(3)	3356	83	0.250(2)
B714C	3	1600	*strong fluorescence*											
B714D	3	1600	3180	39	0.048(2)	3233	60	0.094(3)	3287	47	0.307(7)	3354	84	0.214(5)

Numbers in parentheses reflect 2σ standard errors in the significant digit from best-fit results.

Fig. 1

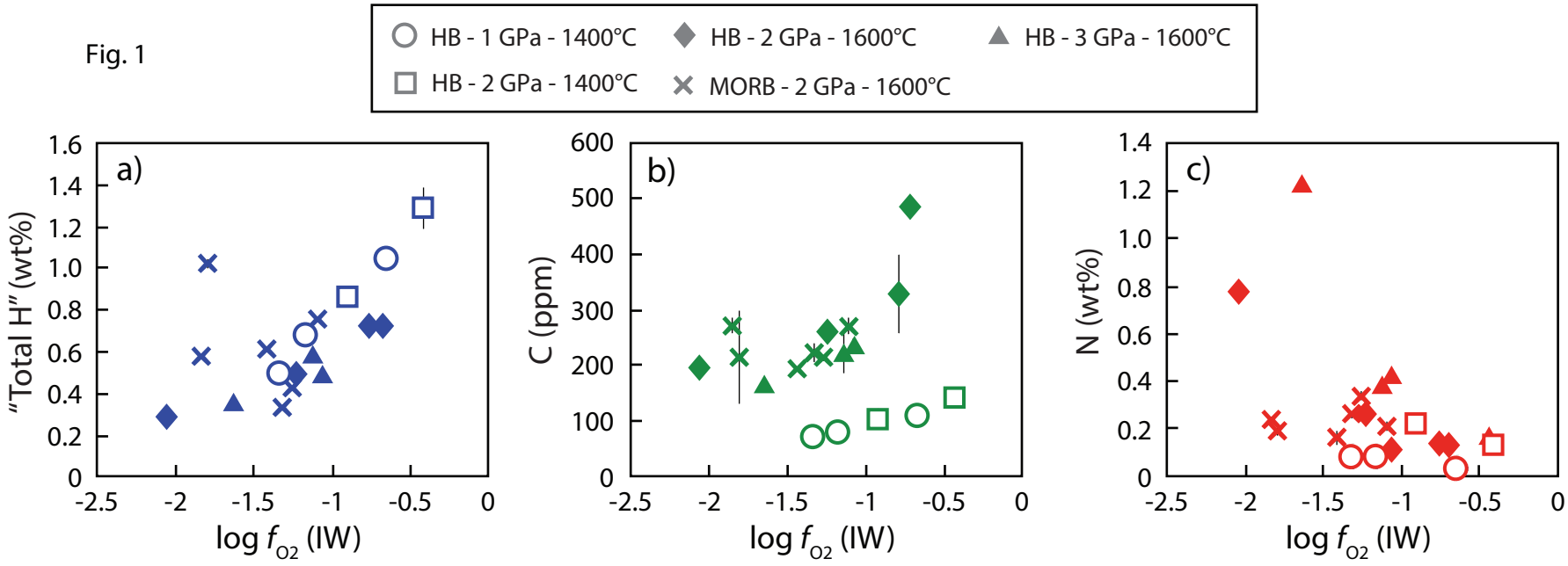
HB - 1 GPa - 1400°C
HB - 2 GPa - 1600°C
HB - 3 GPa - 1600°C
HB - 2 GPa - 1400°C
MORB - 2 GPa - 1600°C
a)
"Total H" (wt%)
log f_{O2} (IW)
b)
C (ppm)
log f_{O2} (IW)
c)
N (wt%)
log f_{O2} (IW)

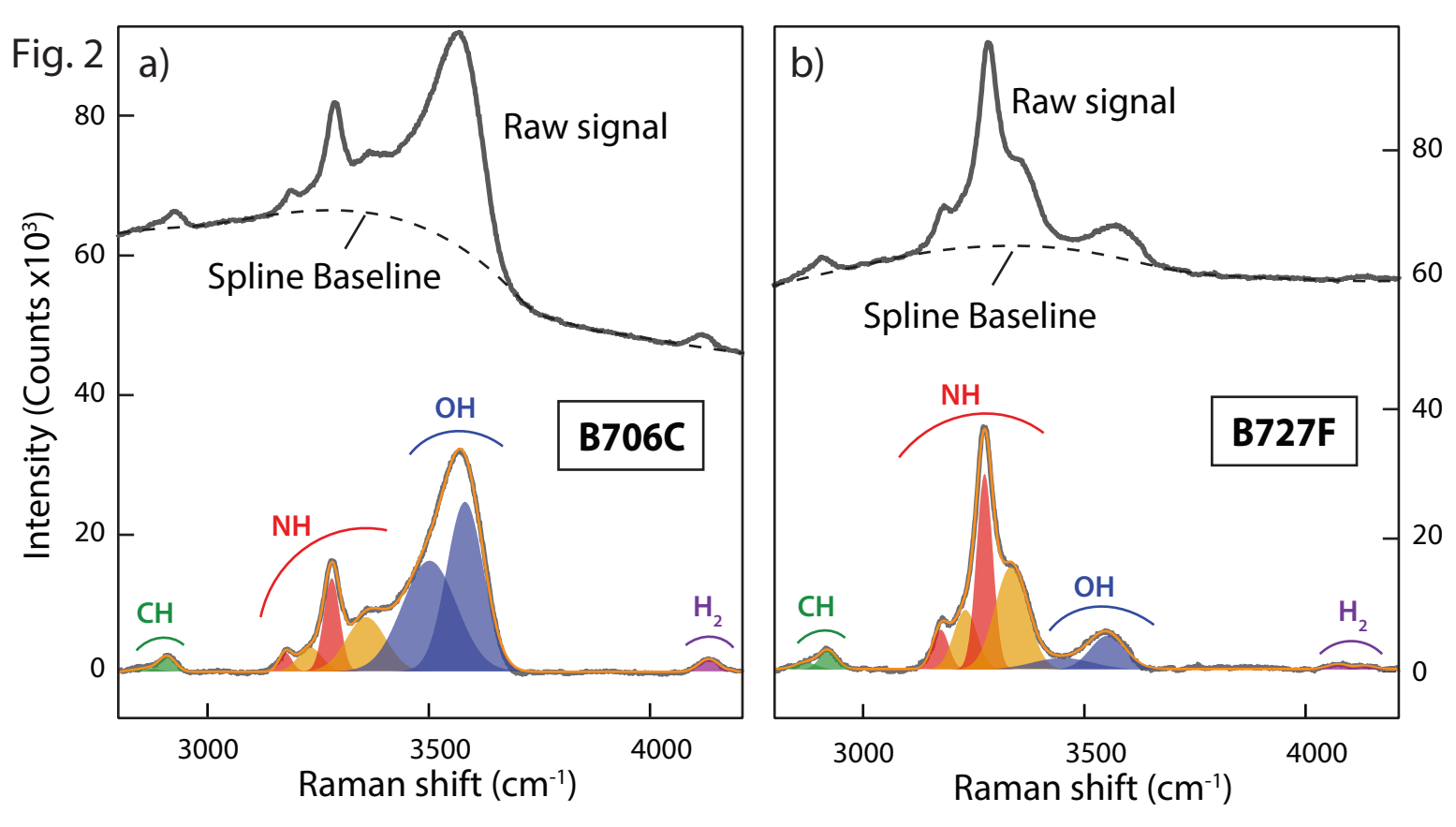
Fig. 2
a)
b)
Raw signal
Spline Baseline
B706C
B727F
NH
OH
CH
H2
Intensity (Counts x10³)
Raman shift (cm⁻¹)
0
20
40
60
80
3000
3500
4000

Fig. 3

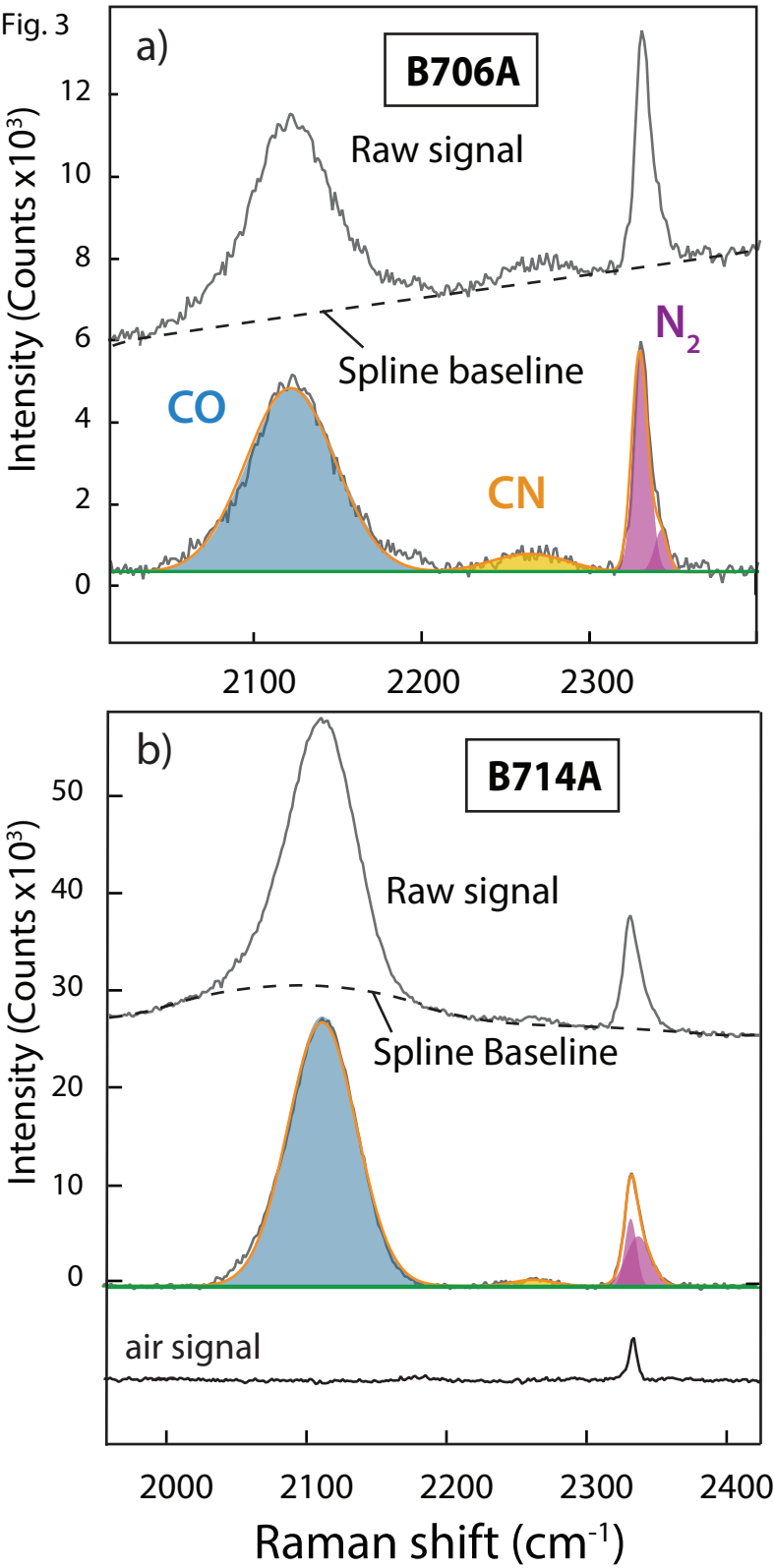
a)
B706A
Raw signal
Spline baseline
CO
CN
N2
Intensity (Counts x10³)
0
2
4
6
8
10
12
2100
2200
2300
b)
B714A
Raw signal
Spline Baseline
air signal
Intensity (Counts x10³)
0
10
20
30
40
50
2000
2100
2200
2300
2400
Raman shift (cm⁻¹)

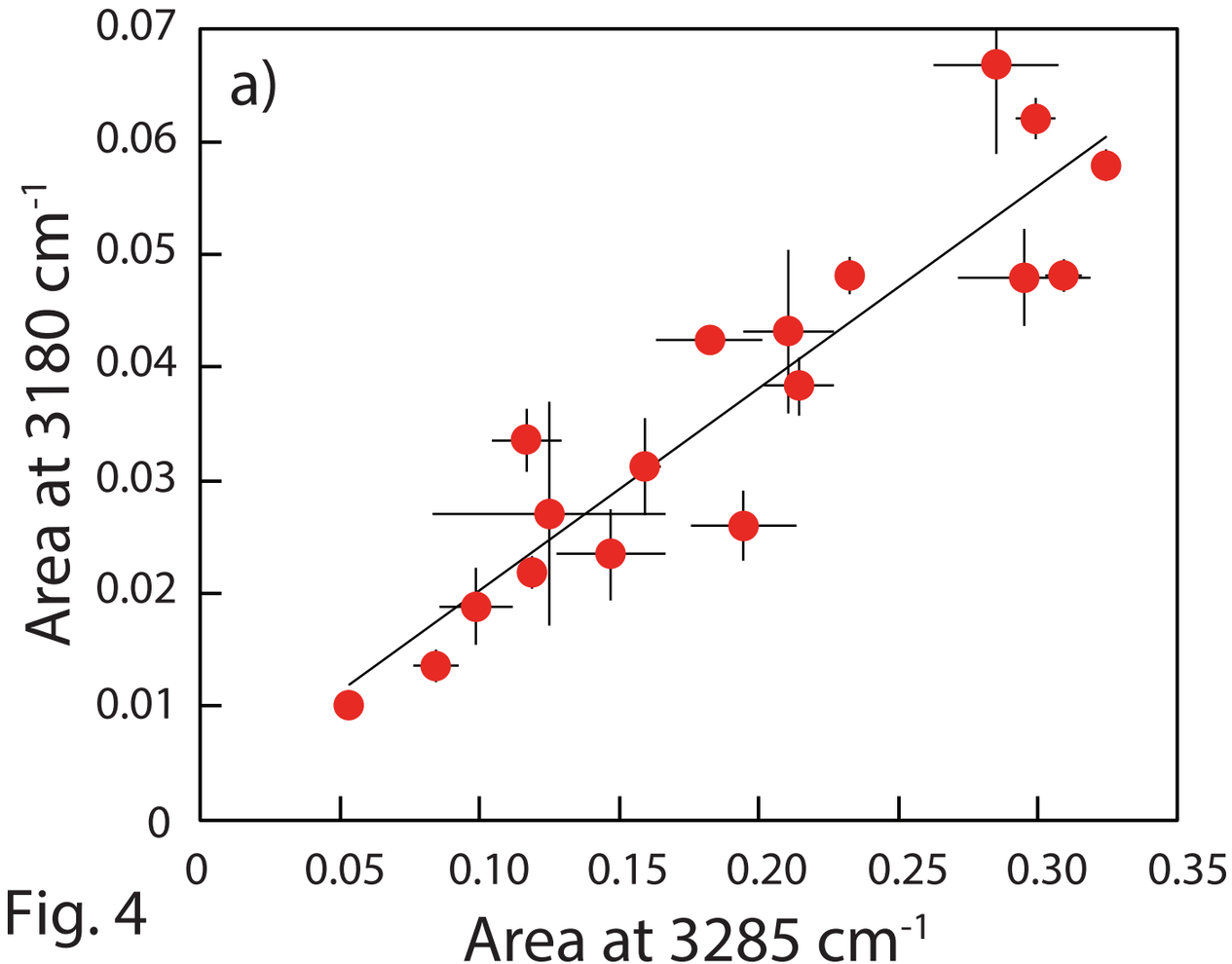
a)
Area at 3180 cm-1
Area at 3285 cm-1
0
0.01
0.02
0.03
0.04
0.05
0.06
0.07
0.05
0.10
0.15
0.20
0.25
0.30
0.35

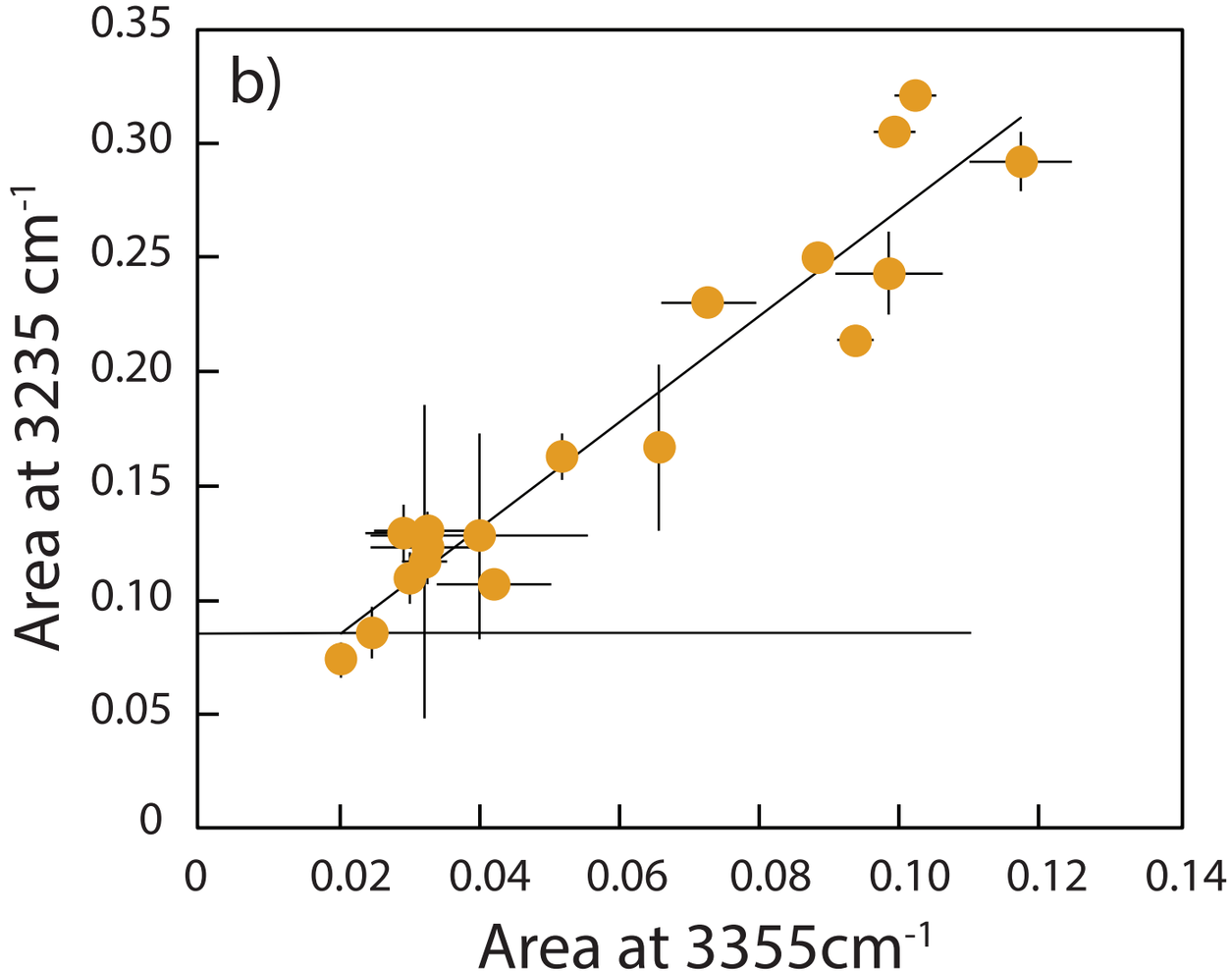
b)
Area at 3235 cm-1
Area at 3355cm-1
0
0.05
0.10
0.15
0.20
0.25
0.30
0.35
0.02
0.04
0.06
0.08
0.10
0.12
0.14

Fig. 4

Fig. 5

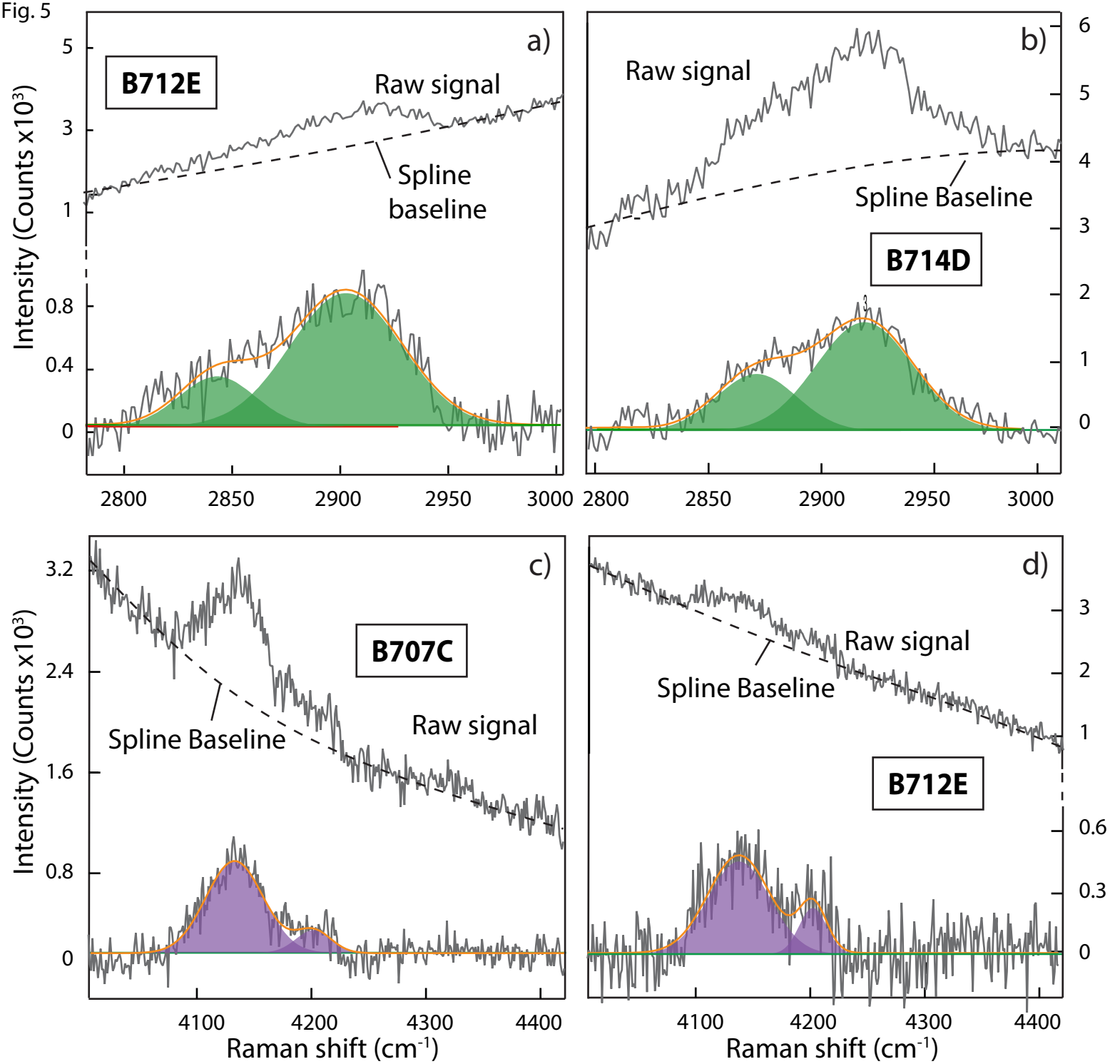
a)
B712E
Raw signal
Spline baseline
b)
Raw signal
Spline Baseline
B714D
c)
B707C
Spline Baseline
Raw signal
d)
Raw signal
Spline Baseline
B712E
Intensity (Counts x10³)
Raman shift (cm⁻¹)

Fig. 6

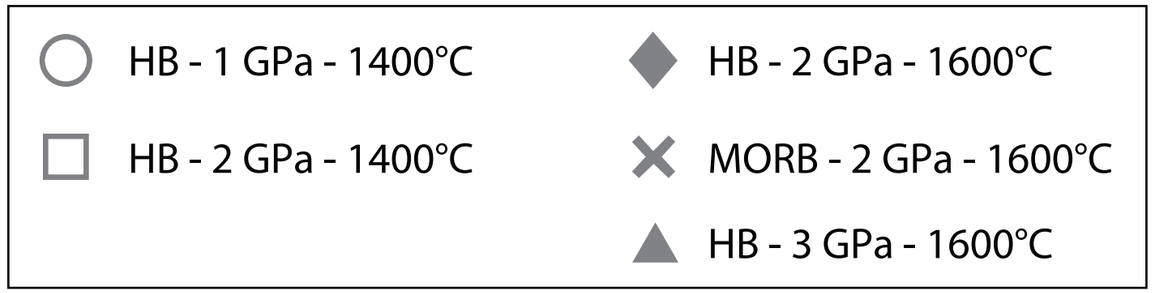
HB - 1 GPa - 1400°C
HB - 2 GPa - 1400°C
HB - 2 GPa - 1600°C
MORB - 2 GPa - 1600°C
HB - 3 GPa - 1600°C

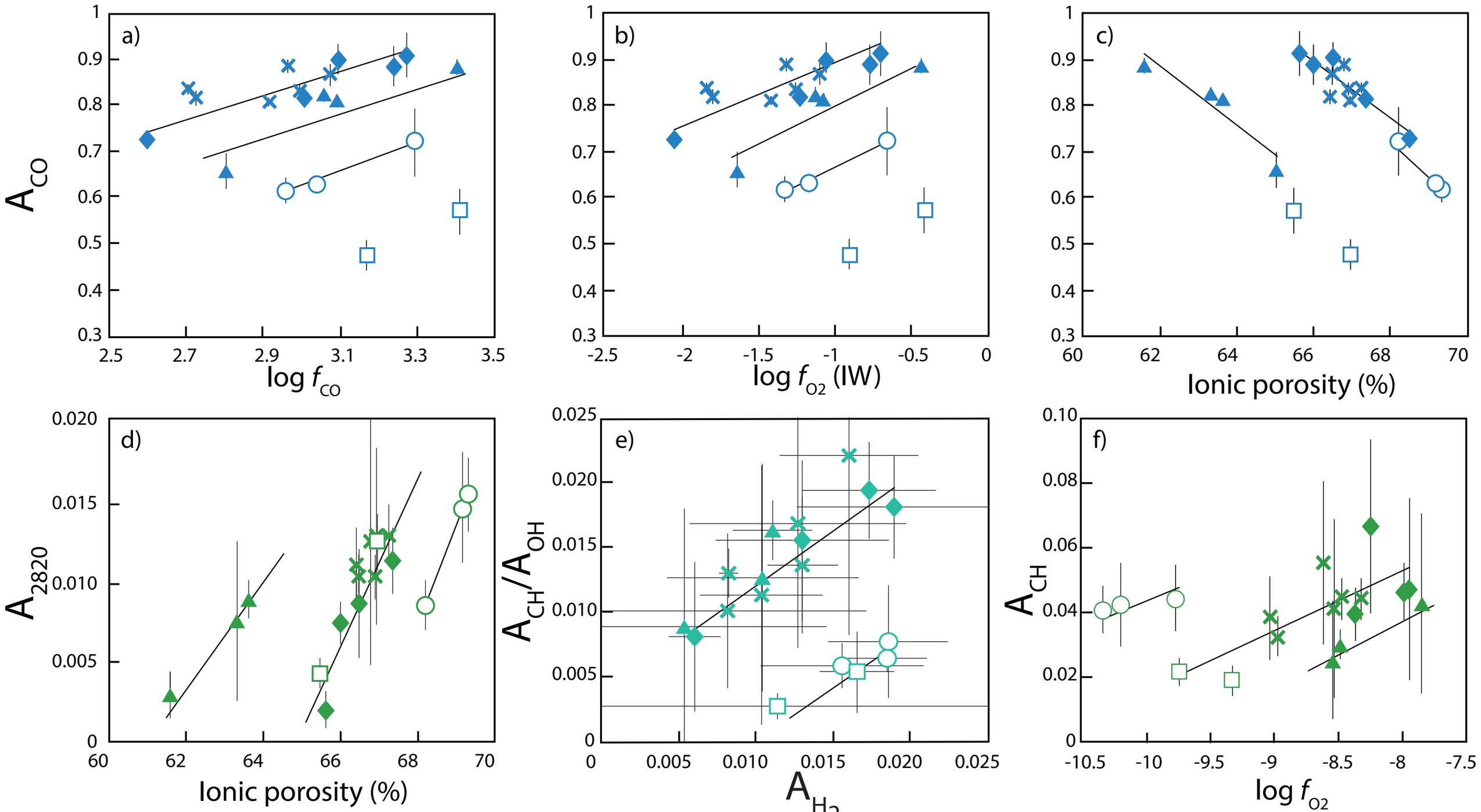
a)
b)
c)
d)
e)
f)
A_{CO}
log f_{CO}
log f_{O2} (IW)
Ionic porosity (%)
A_{2820}
A_{CH}/A_{OH}
A_{H_2}
A_{CH}
log f_{O2}

Fig. 7

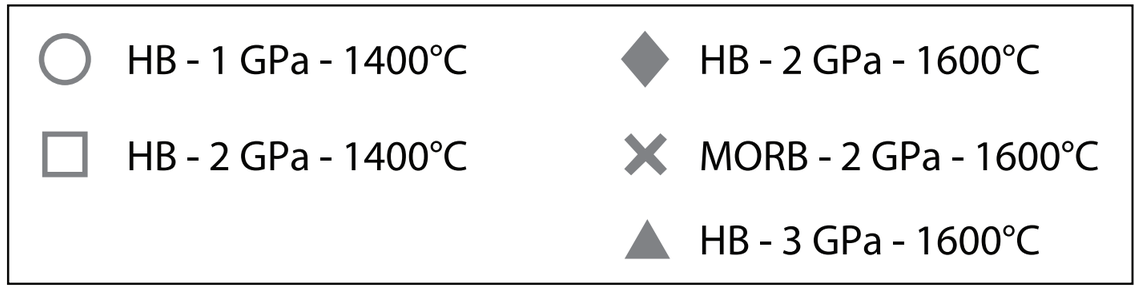
HB - 1 GPa - 1400°C
HB - 2 GPa - 1400°C
HB - 2 GPa - 1600°C
MORB - 2 GPa - 1600°C
HB - 3 GPa - 1600°C

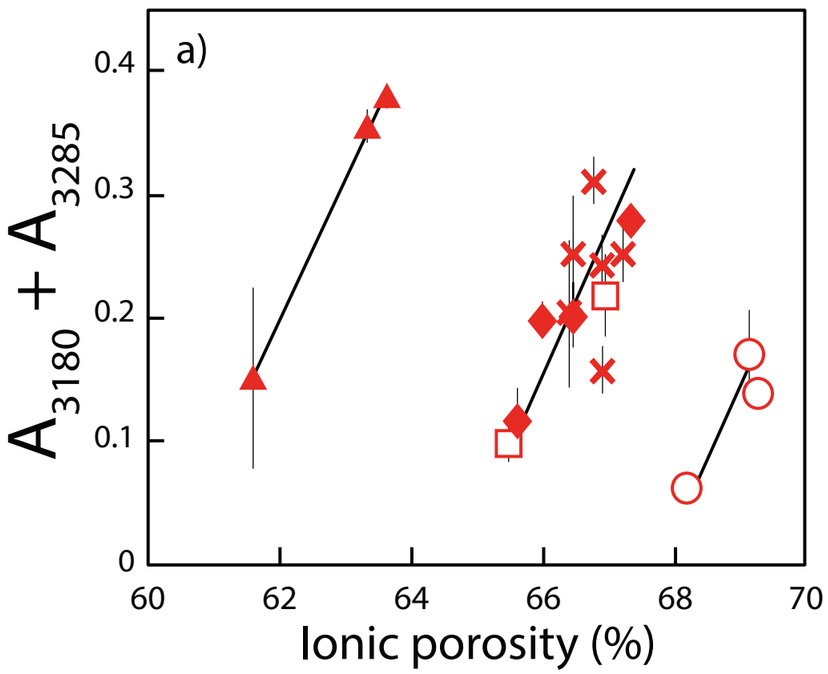
a)
$A_{3180} + A_{3285}$
Ionic porosity (%)

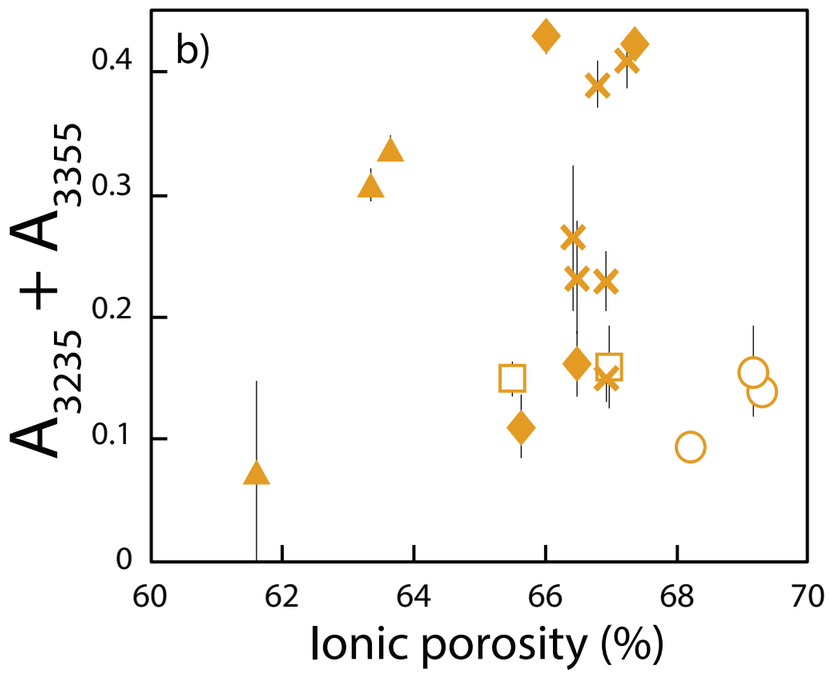
b)
$A_{3235} + A_{3355}$
Ionic porosity (%)

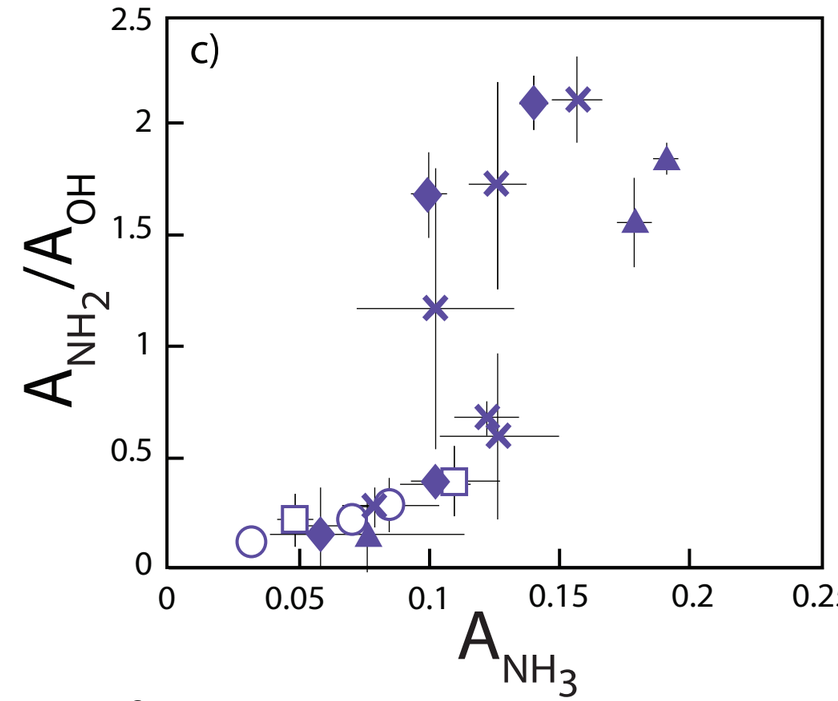
c)
A_{NH_2}/A_{OH}
A_{NH_3}

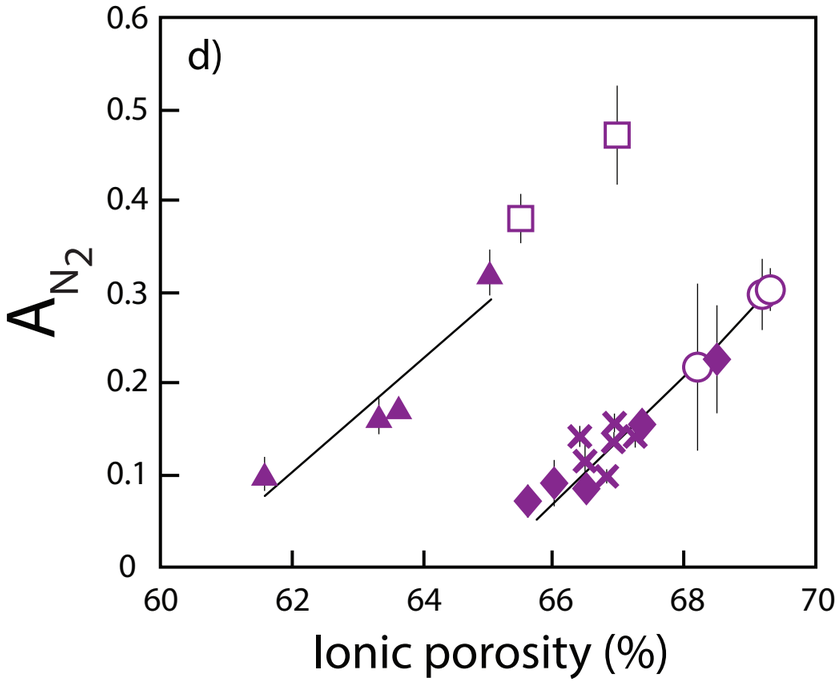
d)
A_{N_2}
Ionic porosity (%)

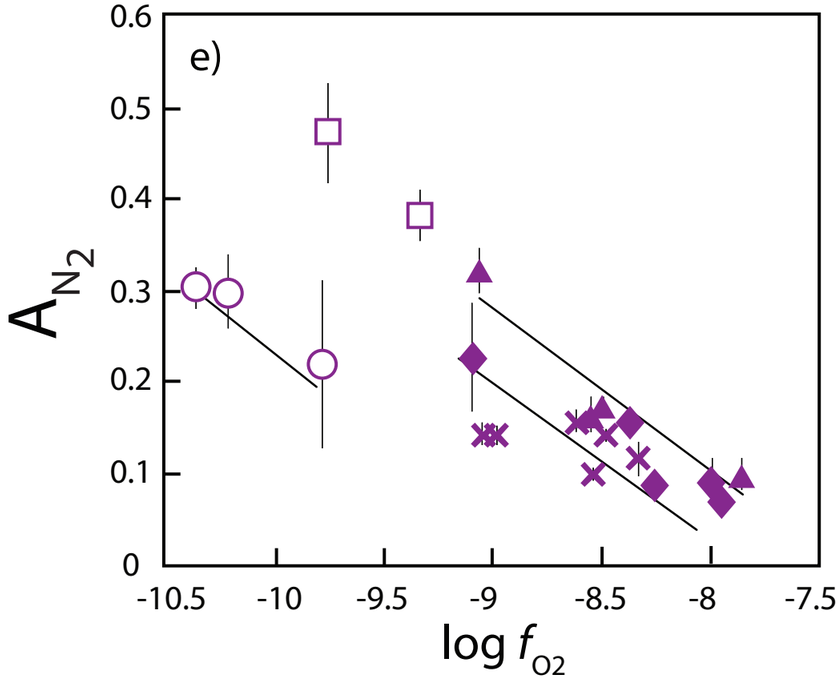
e)
A_{N_2}
log f_{O2}

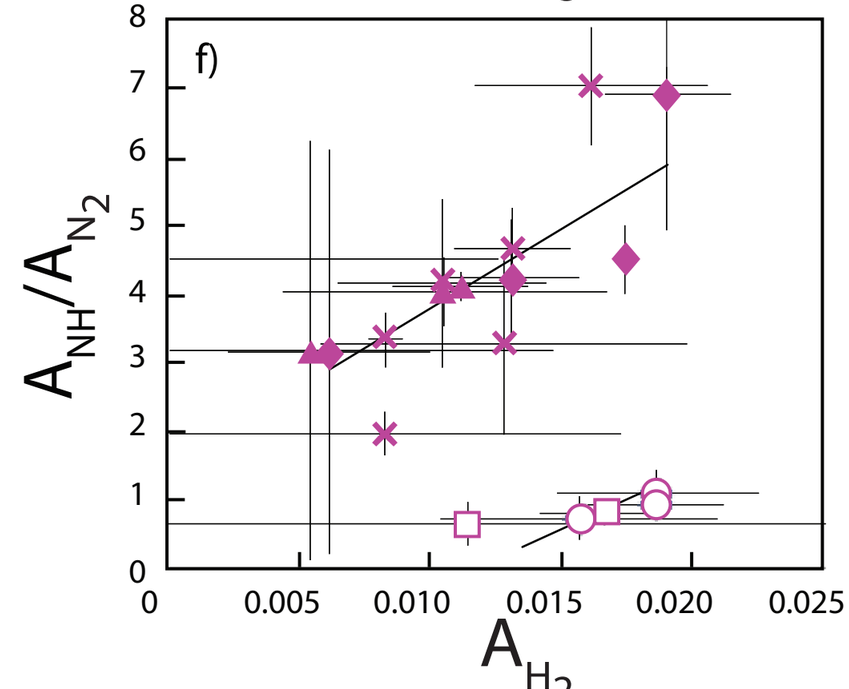
f)
A_{NH}/A_{N_2}
A_{H_2}